

Effects of low-viscous layers and a non-zero obliquity on surface stresses induced by diurnal tides and non-synchronous rotation: The case of Europa

Hermes M. Jara-Oru  *, Bert L.A. Vermeersen

Faculty of Aerospace Engineering, Delft University of Technology, Kluyverweg 1, 2629 HS Delft, The Netherlands

ARTICLE INFO

Article history:

Received 17 January 2011

Revised 16 May 2011

Accepted 26 May 2011

Available online 6 June 2011

Keywords:

Europa

Tides, solid body

Geophysics

Interiors

ABSTRACT

In this study we present a semi-analytical Maxwell-viscoelastic model of the variable tidal stress field acting on Europa's surface. In our analysis, we take into account surface stresses induced by the small eccentricity of Europa's orbit, the non-zero obliquity of Europa's spin axis – both acting on a diurnal 3.55-days timescale – and the reorientation of the ice shell as a result of non-synchronous rotation (NSR). We assume that Europa's putative ocean is covered by an ice shell, which we subdivide in a low-viscous and warm lower ice layer (asthenosphere, viscosity 10^{12} – 10^{17} Pa s), and a high-viscous and cold upper ice layer (lithosphere, viscosity 10^{21} Pa s).

Viscoelastic relaxation influences surface stresses in two ways: (1) through viscoelastic relaxation in the lithosphere and (2) through the viscoelastic tidal response of Europa's interior. The amount of relaxation in the lithosphere is proportional to the ratio between the period of the forcing mechanism and the Maxwell time of the high-viscous lithosphere. As a result, this effect is only relevant to surface stresses caused by the slow NSR mechanism. On the other hand, the importance of the viscoelastic response on surface stresses is proportional to the ratio between the relaxation time (τ_j) of a given viscoelastic mode j and the period of the forcing function. On a diurnal timescale the fast relaxation of transient modes related to the low viscosity of the asthenosphere can alter the magnitude and phase shift of the diurnal stress field at Europa's surface. The effects are largest, up to 20% in magnitude and 7° in phase for ice rigidities lower than 3.487 GPa, when the relaxation time of the aforementioned transient modes approaches the inverse of the average angular rate of Europa's orbit. On timescales relevant for NSR ($>10^4$ years) the magnitude and phase shift of NSR surface stresses can be affected by viscoelastic relaxation of the ocean–ice boundary. This effect, however, becomes only important when the behavior of the lithosphere w.r.t. NSR approaches the fluid limit, i.e. for strong relaxation in the lithosphere. The combination of NSR and diurnal stresses for different amounts of viscoelastic relaxation of NSR stresses in the lithosphere leads to a large variety of global stress fields that can explain the formation of the large diversity of lineament morphologies observed on Europa's surface. Variation of the amount of relaxation in the lithosphere is likely due to changes in the spin rate of Europa and/or the rheological properties of the surface.

In addition, we show that a small obliquity ($<1^\circ$) can have a considerable effect on Europa's diurnal stress field. A non-zero obliquity breaks the symmetric distribution of stress patterns with respect to the equator, thereby affecting the magnitude and orientation of the principal stresses at the surface. As expected, increasing the value of Europa's obliquity leads to larger diurnal stresses at the surface, especially when Europa is located 90° away from the nodes formed by the intersection of its orbital and equatorial planes.

  2011 Elsevier Inc. All rights reserved.

1. Introduction

The determination of Europa's second-degree gravitational coefficients J_2 and C_{22} from the Doppler shift of Galileo's radio signal during four close flybys has allowed us to have a better understanding about the internal structure of this peculiar icy moon.

Under the assumption of hydrostatic equilibrium, the measured values for J_2 and C_{22} imply a differentiated interior consisting of at least three material layers: a Fe or Fe–FeS metallic core, a silicate mantle and a 80–170 km thick H₂O layer (Anderson et al., 1998; Sohl et al., 2002; Schubert et al., 2009). Due to the similar densities of liquid water and solid ice, it is not possible to determine unambiguously from the gravity data whether Europa's H₂O shell is subdivided into a global liquid ocean and an overlying ice shell (Anderson et al., 1998; Sohl et al., 2002). However, the existence of a global subsurface ocean below Europa's ice shell is essentially

* Corresponding author.

E-mail addresses: h.m.jaraorue@tudelft.nl (H.M. Jara-Oru  ), l.l.a.vermeersen@tudelft.nl (B.L.A. Vermeersen).

confirmed by the detection of an induced magnetic field by Galileo's magnetometer (Khurana et al., 1998; Kivelson et al., 2000; Zimmer et al., 2000; Hand and Chyba, 2007; Schilling et al., 2007), and by the existence of a complex network of intersecting cracks, bands and ridges on Europa's surface (e.g. Geissler et al., 1998; Greeley et al., 1998; Hoppa et al., 1999b,c; Pappalardo et al., 1999; Kattenhorn and Hurford, 2009). Europa's liquid ocean would be in direct contact with the underlying silicates, as the pressure at the rock-water interface is too low for the formation of high-pressure ice phases (e.g. Sotin and Tobie, 2004). The currently undetected, but plausible, existence of hydrothermal sea-floor systems would then allow for a mechanism to supply energy and nutrients to Europa's ocean (Hand et al., 2009), increasing the habitability potential of this Jovian moon.

The formation of tectonic features (cracks, bands and ridges) has been attributed to various sources of stresses acting at different timescales. On a 3.55-days timescale, stresses at the icy surface are induced by the diurnal tides induced by the non-zero eccentricity of Europa's orbit (Greenberg et al., 1998, 2003; Hoppa et al., 1999b,c; Harada and Kurita, 2006; Wahr et al., 2009), the non-zero obliquity of Europa's spin axis (Bills, 2005; Hurford et al., 2009; Rhoden et al., 2010, 2011), and physical librations of a decoupled shell (Van Hoolst et al., 2008; Rhoden et al., 2010). Diurnal stresses have been mainly used to model the formation of cycloidal features (Hoppa et al., 1999b; Hurford et al., 2007, 2009; Rhoden et al., 2010) and strike-slip faults (Hoppa et al., 1999c; Preblich et al., 2007; Rhoden et al., 2011) on Europa's surface. On a much longer timescale, stresses may be induced by true polar wander (TPW) of the spin axis with respect to the icy surface (Ojakangas and Stevenson, 1989a; Leith and McKinnon, 1996; Matsuyama and Nimmo, 2008; Schenk et al., 2008) and/or by non-synchronous rotation (NSR) of a decoupled shell (Leith and McKinnon, 1996; Greenberg et al., 1998, 2003; Kattenhorn, 2002; Hurford et al., 2007; Harada and Kurita, 2007; Wahr et al., 2009). These slow stressing mechanisms lead to large (\sim MPa) stresses, which have been used to model the formation of global-scale surface features (Leith and McKinnon, 1996; Geissler et al., 1998; Greenberg et al., 1998; Schenk et al., 2008). In addition, large isotropic stresses (up to \sim 10 MPa) can result from thickening of the ice shell (Nimmo, 2004).

Diurnal stresses acting on Europa's surface have been usually computed by means of the thin shell approximation (Leith and McKinnon, 1996; Greenberg et al., 1998; Hoppa et al., 1999b; Hurford et al., 2007, 2009; Rhoden et al., 2010, 2011). In this method, which is based on the work of Melosh (1980), Europa is assumed to be a thin elastic icy shell floating on a global liquid ocean (Hurford et al., 2007). A more realistic model by Harada and Kurita (2006) analyzes the influence of a differentiated internal structure on the surface diurnal stress, focusing on the relation between the magnitude of surface stresses and the thickness of the material layers. Harada and Kurita (2006) shows that surface diurnal stresses only depend on the thickness of the ice shell, hence supporting the assumption made by the thin shell approximation regarding the effect of the deep interior. The methods discussed above inherently assume that Europa's ice shell behaves elastically when forced by diurnal tides. However, as suggested by thermal models (e.g. Hussmann et al., 2002; Tobie et al., 2003) and impact crater models (Schenk, 2002), the lower portion of Europa's ice shell most probably behaves in a viscoelastic way under the influence of diurnal tides. Recent modeling by Wahr et al. (2009) includes the effect of viscoelasticity on surface diurnal stresses, thereby offering a potential method to study the effect of such a layer. However, the discussion in Wahr et al. (2009) only focus on cases for which Europa's interior behaves nearly elastically with respect to diurnal tides.

Europa's decoupled ice shell can experience slow non-synchronous rotation as a result of the acting tidal torque and lateral thick-

ness variations in the shell (Greenberg and Weidenschilling, 1984; Ojakangas and Stevenson, 1989b; Bills et al., 2009). If existing, NSR would be a slow periodic process with a period ($>11,000$ years) comparable to the characteristic Maxwell time (τ_M = viscosity/rigidity) of the lithospheric shell (see Section 6). Hence, viscoelastic relaxation in the lithospheric shell is expected to have an important influence on the magnitude and orientation of NSR stresses at Europa's surface. Nevertheless, NSR stresses acting on Europa's surface have been often computed through application of the thin shell approximation to determine the elastic stress fields induced by the current tidal bulge and by the original tidal bulge (Leith and McKinnon, 1996; Greenberg et al., 1998; Hurford et al., 2007). The rotation angle between the two elastic stress fields, usually referred to as the accumulated degrees of NSR, defines the amount of NSR stress that accumulates in the shell (e.g. Greenberg et al., 1998). More realistic models of surface NSR stresses by Harada and Kurita (2007) and Wahr et al. (2009) have focused on the determination of the stress directly from the Maxwell viscoelastic equations of motion and the acting NSR tidal potential. This kind of modeling has two main advantages with respect to the simpler thin shell approximation: (1) it includes viscoelastic relaxation effects into the computation of NSR stresses and (2) it allows to relate the obtained stress field to the rheological properties of the interior. Both aforementioned studies obtain similar results for the relation between the simulated NSR stress and the rheological properties of the icy shell. However, both studies take a different approach to analyze the effect of viscoelastic relaxation on surface NSR stresses. The work by Harada and Kurita (2007) constrains the magnitude of diurnal and NSR stresses to be comparable, as previously suggested by Greenberg et al. (1998). As a result, Harada and Kurita (2007) implicitly assume that NSR stresses are severely affected by viscoelastic relaxation in the lithospheric shell. This assumption inherently leads to a westward shift of 45° in the surface distribution of the NSR stress field; the same as the one predicted in Greenberg et al. (1998). On the other hand, the work by Wahr et al. (2009) takes into consideration that NSR stresses could be larger in magnitude than diurnal stresses. Therefore, the westward shift of the NSR stress field does not necessarily have to be equal to 45° . This conclusion has a large effect on the determination of the time elapsed since the formation of a surface feature (Wahr et al., 2009), especially if the relaxation state of the NSR stress field changes with time.

Although the studies by Harada and Kurita (2007) and Wahr et al. (2009) already discussed the influence of viscoelasticity on surface stresses, their treatment is mostly focused on NSR stresses. Viscoelastic effects on diurnal stresses have often been neglected by considering quasi-elastic interior models. However, thermal models of Europa's ice shell have often assumed that the lower convective portion of the ice (asthenosphere) has a Newtonian viscosity in the range 1.0×10^{13} – 1.0×10^{15} Pa s (see e.g. Hussmann et al., 2002; Sotin and Tobie, 2004; Nimmo and Manga, 2009). In this range, not only tidal heat dissipation becomes largest but also the viscoelastic effect on diurnal stresses. As a result, we aim to extend the determination of diurnal stresses to interior models with a 2-layered ice shell, in which the Maxwell time of the lower icy sublayer is smaller or comparable to the orbital period, as suggested by thermal modeling. In addition we will take into account the effect of a non-zero obliquity on diurnal stresses from a viscoelastic perspective. Regarding NSR stress modeling, we will discuss the effect of the viscosity of the lower ice layer as a function of the amount of relaxation. In addition, we allow NSR stresses to be larger, comparable and smaller than diurnal stresses in order to infer the possible relation between the resulting NSR-diurnal stress field and the observed features.

The viscoelastic modeling of tidal stresses on Europa's surface is based on three aspects: determination of the tidal forcing

(Section 2), assumptions on Europa's internal configuration (Section 3) and determination of Europa's viscoelastic response to tidal forces (Section 4). In Section 2, we present analytical expressions for the diurnal and NSR tidal potential, in which we include the effect of a non-zero obliquity. In Section 3, we define our reference 5-layer model of Europa's interior. In Section 4, we discuss an alternative method to determine the tidal Love numbers of Maxwell viscoelastic planets with an internal ocean. This method, which is derived from normal mode techniques applied to postglacial rebound and true polar wander on Earth, subdivides the non-elastic response into several relaxation modes, each of them characterized by a specific relaxation time and strength. In Section 5, we use the tools presented in Sections 2–4 to develop an analytical representation of diurnal and NSR stresses acting on Europa's surface. Thereafter, in Section 6, we analyze the relation between diurnal/NSR stresses and the physical properties of the interior. We show there that the magnitude of diurnal stresses mainly depends on the presence of an ocean and the rigidity of ice-I, while the spatial distribution of the stress patterns at the surface primarily depends on the obliquity of the Europa's spin axis and the viscosity and thickness of the asthenosphere. On the other hand, NSR stresses are most influenced by the rheological properties of the lithosphere and the unknown frequency of the non-synchronous motion of the ice shell. Finally, in Section 7 we combine the results obtained in Section 6 for diurnal and NSR stresses. We suggest that time variations in the relative importance of NSR stresses with respect to diurnal stresses could theoretically lead to the wide variety of lineament morphologies observed on Europa's icy surface.

2. The tidal potential

The shape and orientation of the tidal bulge would remain fixed to the satellite's figure if the satellite would always show exactly the same face to the tide-raising planet. This particular configuration would take place if: (1) the satellite's orbit around the planet would be circular (zero eccentricity), (2) the spin axis of the satellite would be perpendicular to its orbital plane (zero obliquity), and (3) the spin rate of the satellite would be synchronous to its orbital motion (synchronous rotation). None of these requirements apply to Europa. First of all, the 1:2:4 Laplace resonance between the orbital motions of Io, Europa and Ganymede prevents the orbit of Europa to become circular. In addition, the obliquity of Europa's spin axis cannot be exactly equal to zero as a consequence of precession of Europa's orbital plane (Bills, 2005). Furthermore, a global subsurface ocean might decouple the rotational motion of Europa's ice shell from the rotational motion of the rocky interior. As a result, the positive net tidal torque experienced by the satellite might only affect the spin rate of the decoupled ice shell whereas the rocky interior remains tidally locked (e.g. Greenberg and Weidenschilling, 1984; Ojakangas and Stevenson, 1989b). Although non-synchronous rotation (NSR) of Europa's ice shell is strongly favored by the orientation of tectonic features (e.g. Greenberg et al., 1998, 2003; Hoppa et al., 2001; Kattenhorn, 2002; Hurford et al., 2007; Rhoden et al., 2010), the torque caused by Jupiter's gravitational attraction on permanent asymmetries in Europa's figure might counteract the net tidal torque and maintain synchronicity of the spin rate (Greenberg and Weidenschilling, 1984; Bills et al., 2009). The contribution of the permanent asymmetries to the evolution of the spin rate depends on the difference between the two principal equatorial moments of inertia (i.e. $B - A$) and the orientation of the longest axis (related to moment of inertia A) with respect to the direction of the planet (see e.g. Goldreich and Peale, 1966).

The tidal force field acting on Europa's surface is subjected to periodic variations on a diurnal timescale (≈ 3.55 days), which

are mainly the result of the slightly elliptical shape of Europa's orbit around Jupiter (with eccentricity $e = 0.0094$). Diurnal changes in the magnitude of the tidal forces acting on Europa, which are caused by periodic variations in the distance between Europa and Jupiter, lead to continuous stretching and squeezing of the tidal bulge. On the other hand, diurnal changes in the orientation of the tidal field with respect to the surface, which are caused by differences between Europa's spin rate and the instantaneous orbital rate, lead to periodic longitudinal migrations of the tidal bulge. In both cases, the materials composing the interior of Europa will continuously try to deform accordingly to the shape dictated by the acting diurnal tidal field. This periodic reshaping of Europa's interior leads to the generation of frictional heat in the interior and ~ 100 kPa stresses at the surface (see Section 6 for a more detailed analysis).

Also on a diurnal timescale, the tidal force field acting on Europa's surface experiences additional periodic variations as the obliquity of Europa's spin axis is non-zero ($\varepsilon \approx 0.1^\circ$). The most important effect of Europa's non-zero obliquity is that it causes diurnal changes in the latitudinal orientation of the tidal bulge. As a result, the obliquity introduces an additional source of heat dissipation in the interior and stresses at the surface of Europa. For example, Europa's non-zero obliquity might have played a substantial role in the formation of cycloidal cracks crossing the equator, as suggested by Hurford et al. (2009).

In addition, the tidal field acting on the surface of Europa might be subjected to (periodic) variations on timescales much larger than one European day. Here we assume that the spin rate of Europa's decoupled ice shell is slightly faster than synchronous, in accordance with the geological evidence (Greenberg et al., 1998, 2003; Hoppa et al., 2001; Kattenhorn, 2002; Hurford et al., 2007; Rhoden et al., 2010). As a consequence, the tidal bulge exerted by Jupiter on Europa would slowly migrate in westward direction with respect to a meridian attached to the icy surface. A complete revolution of the tidal bulge with respect to Europa's surface (i.e. the period of NSR) would take more than 12,000 years (Hoppa et al., 1999a). Non-synchronous rotation is a very important process in the analysis of surface stresses for two reasons: (1) it might be a source of large \sim MPa stresses (Harada and Kurita, 2007; Wahr et al., 2009) and (2) it changes the longitude of tectonic features. NSR stresses have been often related to the formation of global lineaments on Europa's surface (see e.g. Greenberg et al., 1998; Harada and Kurita, 2007; Hurford et al., 2007; Wahr et al., 2009).

Tidal forces are usually expressed as the gradient of a scalar field, the tidal potential Φ_T , which can be expressed as a series of spherical harmonics

$$\Phi_T = GM_T \frac{1}{a} \sum_{l=2}^{\infty} \left(\frac{R}{a} \right)^l P_l(\cos \psi), \quad (1)$$

where G , M_T , R and a are defined as the universal gravitational constant, the mass of the primary, the mean radius of Europa and the distance to the primary, respectively. The function P_l is defined as the Legendre polynomial of spherical harmonic degree l . The angle ψ is the angular distance of a point on the surface with respect to the line connecting the centers of Europa and Jupiter. The series of spherical harmonics given by Eq. (1) converges rapidly as the term $(R/a)^l$ decreases exponentially when the harmonic degree l increases. In the case of Jupiter's tide on Europa, the contribution of the second degree term is already about 430 times larger than the contribution of the third degree term. Hence, we can safely express the tidal potential exerted by Jupiter on Europa by only taking into account the second degree term.

Thereafter, we apply the method of Kaula (1964) to express the tidal potential in terms of the Keplerian elements describing the motion of Jupiter w.r.t. a reference frame attached to Europa's

rotating surface, in which the z -axis coincides with Europa's spin axis and the x -axis points towards Jupiter at pericenter. We simplify the resulting expression by taking into account that Europa's eccentricity and obliquity are small, i.e. we consider terms only up to first order in eccentricity and obliquity and neglect any cross terms of the eccentricity and obliquity. Moreover, we neglect the effect of NSR on the eccentricity tide and obliquity tide because these terms are approximately two orders of magnitude smaller than the effect of NSR on the main "static" tide. Then, the resulting expression for the tidal potential Φ_T exerted by Jupiter on Europa becomes

$$\Phi_T = (nR)^2 \left\{ \Phi_T^0 + \Phi_T^{ns} + \Phi_T^{e1} + \Phi_T^{e2} + \Phi_T^{o1} \right\}, \quad (2)$$

where

$$\Phi_T^0 = -\frac{1}{2}P_{2,0}^\theta + \frac{1}{4}P_{2,2}^\theta \cos(2\phi), \quad (3)$$

$$\Phi_T^{ns} = -\frac{1}{2}P_{2,2}^\theta \sin(2\phi + \Omega_{ns}t) \sin(\Omega_{ns}t), \quad (4)$$

$$\Phi_T^{e1} = -\frac{3e}{2}P_{2,0}^\theta \cos(nt), \quad (5)$$

$$\Phi_T^{e2} = \frac{e}{4}P_{2,2}^\theta [3 \cos(2\phi) \cos(nt) + 4 \sin(2\phi) \sin(nt)], \quad (6)$$

$$\Phi_T^{o1} = P_{2,1}^\theta \cos(\varepsilon) \sin(\varepsilon) \cos(\phi) \sin(\omega + nt), \quad (7)$$

where e and n are respectively the eccentricity and the mean motion of Europa's orbit, ε is the obliquity of Europa's spin axis and ω is the argument of pericenter measured w.r.t. the ascending node where Europa's orbital plane crosses Europa's equatorial plane. The variable Ω_{ns} describes the constant angular rate of NSR, i.e. the difference between Europa's angular spin rate and Europa's mean orbital rate. The numerical values corresponding to the aforementioned parameters are listed in Table 1. Furthermore, the angles θ and ϕ are, respectively, the colatitude and longitude of a point on Europa's surface. Finally, the associated Legendre polynomials $P_{2,0}^\theta$, $P_{2,1}^\theta$ and $P_{2,2}^\theta$ are defined by

$$P_{2,0}^\theta = \frac{3 \cos^2(\theta) - 1}{2}, \quad (8)$$

$$P_{2,1}^\theta = 3 \sin(\theta) \cos(\theta), \quad (9)$$

$$P_{2,2}^\theta = 3 \sin^2(\theta). \quad (10)$$

Eqs. (2)–(7) show that the tidal potential acting on Europa consists of a static component and several time-dependent components. The term Φ_T^0 represents the time invariant potential, although the second term of Eq. (3) would contain a time variable component if physical librations of the ice shell (Van Hoolst et al., 2008; Baland and Van Hoolst, 2010) would be taken into account. The term Φ_T^0 would completely define the tidal potential acting on Europa's surface if Europa's orbit would be circular, its rotation synchronous and its obliquity zero. In that particular case, the stresses induced by the formation of the bulge would have had suf-

ficient time to relax completely and tidal heat would not be dissipated in the interior of Europa. The term Φ_T^{ns} describes the contribution of NSR to the tidal potential. This term is only non-zero and time dependent if the ice shell rotates non-synchronously with respect to the orbital motion, i.e. when $\Omega_{ns} \neq 0$. Finally, the terms Φ_T^{e1} , Φ_T^{e2} and Φ_T^{o1} represent the diurnal tidal potential resulting from the non-zero eccentricity of Europa's orbit (first two terms) and the non-zero obliquity of Europa's spin axis (last term).

3. The interior of Europa

The materials composing the interior of Europa and other planetary satellites do not respond in a perfectly elastic way to the acting tidal forces at either diurnal timescales nor at timescales relevant to NSR. Part of the interior's response is delayed with respect to the onset time of the tidal forcing as a result of viscous relaxation effects. Therefore, the interior of a planetary satellite will most probably behave as a viscoelastic body rather than as a purely elastic or fluid body (see e.g. Tobie et al., 2005). In this paper, the Maxwell viscoelastic model has been adopted to describe the rheological behavior of Europa's interior. An important parameter in the definition of the Maxwell model is the ratio between the viscosity η and the rigidity μ of the material under deformation. This ratio, the so-called Maxwell time $\tau_M = \eta/\mu$, gives an indication of the time at which the material shows a transition from elastic behavior to viscous behavior. At short-term timescales, i.e. $t \ll \tau_M$, the Maxwell model describes the interior as an elastic body, whereas at long-term timescales, i.e. $t \gg \tau_M$, the interior is described as a fluid body (Sabadini and Vermeersen, 2004).

The internal structure of Europa has been assumed to consist of five homogeneous and incompressible spherical layers: a fluid metallic core of Fe and/or FeS, a large silicate mantle, a liquid ocean, a warm low-viscous ice-I layer and a cold high-viscous ice-II layer on top. The radius r and density ρ of each of these concentric spherical layers needs to be such that the complete model of Europa's interior satisfies the conditions on average density ($\rho_{av} = 2989 \text{ kg m}^{-3}$) and normalized mean moment of inertia ($\frac{I}{MR^2} = 0.346$) (Anderson et al., 1998). The methodology used in this paper to model the layered structure of Europa's interior follows the approach outlined in Sohl et al. (2002) and Harada and Kurita (2006).

Although the entire ice shell is assumed to have a constant density ρ and rigidity μ , we subdivide the ice shell in two layers with different viscosities η . The introduced viscosity contrast leads to the existence of two ice layers with different mechanical and thermal properties (viscosity is a function of temperature). The subdivision of the ice shell in two layers is consistent with thermal models dealing with stagnant lid convection in the ice shell (e.g. Hussmann et al., 2002; Tobie et al., 2003) and with the morphology of impact craters on Europa's surface (Schenk, 2002).

In this paper, we will make use of various models of Europa's interior to analyze the relation between tidal stresses at the surface and the parameters defining the interior. To reduce the number of

Table 1
Physical parameters: tidal potential acting on Europa.

Parameter	Symbol	Value	Unit	Reference
Mean radius	R	1562	km	Seidelmann et al. (2007)
Mean motion	n	101.37472	degree/day	Bills (2005)
Eccentricity	e	0.0094	–	Wahr et al. (2009)
Obliquity	ε	0.1	degree	Bills (2005)
Argument of pericenter	ω	345	degree	Hurford et al. (2009)
Angular rate of NSR	Ω_{ns}	<0.03	degree/year	Hoppa et al. (1999a)
Period of NSR	T_{ns}	>12,000	years	Hoppa et al. (1999a)

Table 2

Reference 5-layer model of Europa's interior.

Layer	Outer radius (km)	Density (kg m ⁻³)	Rigidity (GPa)	Viscosity (Pa s)
Lithosphere	1562	937.0	3.487	1.0 × 10 ²¹
Asthenosphere	1557	937.0	3.487	1.0 × 10 ¹⁴
Ocean	1532	1000.0	0	0
Silicate mantle	1432	3453.6	65.000	1.0 × 10 ¹⁹
Core	600	5565.8	0	0

plausible models, we do not change the size of the core (600 km), the thickness of the H₂O layer (130 km), the thickness of the lithosphere (5 km), the densities of ice and liquid water (937 kg m⁻³ and 1000 kg m⁻³, respectively), the rigidity of the silicate mantle (65 GPa), and the viscosities of the mantle and the lithosphere (1.0 × 10¹⁹ Pa s and 1.0 × 10²¹ Pa s, respectively). We vary the total thickness of the ice shell from 5 km to 130 km (no ocean), the rigidity of ice-I from 1 GPa to 10 GPa, and the viscosity of the asthenosphere from 1.0 × 10¹² Pa s to 1.0 × 10¹⁷ Pa s. However, we will limit the graphical representation of spatial and temporal variations of surface stresses to our standard model of Europa's interior, which is defined by the physical parameters listed in Table 2.

4. The impulse tidal response of Europa

4.1. Classical method

In agreement with the correspondence principle (Peltier, 1974), the tidal response of a spherical, self-gravitating and radially stratified Maxwell viscoelastic planet can be retrieved from the solution of the equivalent elastic problem either in the Fourier or Laplace domain. There are a few differences between the two approaches, all of them having their origin in the definition of the viscoelastic Lam  parameters $\tilde{\mu}$ and $\tilde{\lambda}$. In the Fourier approach, the Lam  parameters are complex functions of frequency and hence the tidal response becomes a complex variable as well. The effect of viscoelasticity on the tidal response is introduced by the imaginary part of the calculated response (i.e. the imaginary Love numbers). In the Laplace approach, on the other hand, the Lam  parameters remain real-valued variables and the effect of viscoelasticity on the tidal response is introduced through the normal modes of the free surface problem (see Appendix A). Each of these normal modes is theoretically related to the relaxation of an internal boundary. Therefore, this approach often leads to a deeper insight into the mechanisms governing the relaxation process (Sabadini and Vermeersen, 2004).

Since the tidal forcing exerted by Jupiter on Europa shows a harmonic behavior, it would seem more appropriate to use the Fourier approach to determine the tidal response of a Maxwell viscoelastic body (see e.g. Moore and Schubert, 2000; Tobie et al., 2005; Harada and Kurita, 2007; Rappaport et al., 2008; Roberts and Nimmo, 2008; Wahr et al., 2009). Nevertheless, in the remaining of this paper we proceed our treatment of the tidal response by means of the Laplace transform. This choice is based on two reasons: (1) to analyze the characteristics of the relaxation process in more detail and (2) to avoid the presence of complex-valued variables prior to the determination of the rotation modes from the linearized Liouville equation (relevant for the treatment of true polar wander).

The response at a radial distance r from the center of the planet is commonly expressed in terms of the radial functions \tilde{y}_1 to \tilde{y}_6 (from here on, the tilde refers to a variable in the Laplace domain), which are defined in the following way (Sabadini and Vermeersen, 2004):

$$\tilde{y}_1 = \tilde{U}_l, \quad (11)$$

$$\tilde{y}_2 = \tilde{V}_l, \quad (12)$$

$$\tilde{y}_3 = 2\tilde{\mu} \frac{\partial \tilde{U}_l}{\partial r} + \tilde{\lambda} \tilde{\chi}_l = \tilde{\sigma}_{rr}, \quad (13)$$

$$\tilde{y}_4 = \tilde{\mu} \left(\frac{\partial \tilde{V}_l}{\partial r} - \frac{\tilde{V}_l}{r} + \frac{\tilde{U}_l}{r} \right) = \tilde{\sigma}_{\theta\theta}, \quad (14)$$

$$\tilde{y}_5 = -\tilde{\Phi}_l, \quad (15)$$

$$\tilde{y}_6 = -\frac{\partial \tilde{\Phi}_l}{\partial r} - \frac{l+1}{r} \tilde{\Phi}_l + 4\pi G \rho_0 \tilde{U}_l = \tilde{Q}_l, \quad (16)$$

where \tilde{U}_l is the radial deformation, \tilde{V}_l is the tangential or lateral deformation, $\tilde{\sigma}_{rr}$ is the radial stress, $\tilde{\sigma}_{\theta\theta}$ is the tangential stress, $-\tilde{\Phi}_l$ is the perturbed gravitational potential and \tilde{Q}_l is the so-called potential stress. Note that we have chosen to use the potential stress \tilde{Q}_l as a radial function rather than the radial derivative of the perturbed potential $\frac{\partial \tilde{\Phi}_l}{\partial r}$. This choice can be explained by the fact that the radial derivative is not continuous at internal boundaries, while the potential stress is. The name ‘‘potential stress’’, however, has no physical meaning and is just a nickname to complement the naming of the stresses defined by Eqs. (13) and (14). All radial functions \tilde{y}_1 to \tilde{y}_6 are characterized by being continuous at the interface between layers.

Furthermore, as shown by expressions (11)–(16), the radial functions depend on the radial distance r , the Laplace parameter s and the degree l of the spherical harmonic expansion. The parameters G , ρ_0 and $\tilde{\chi}_l$ are defined as the universal gravitational constant, the unperturbed density of the material and the divergence of the displacement field or dilatation. The Laplace-transformed compliances $\tilde{\mu}$ and $\tilde{\lambda}$ are defined by

$$\tilde{\mu} = \frac{\mu s}{s + \frac{\mu}{\eta}}, \quad (17)$$

and

$$\tilde{\lambda} = \frac{(\kappa - \frac{2}{3}\mu)s + \frac{\mu}{\eta}\kappa}{s + \frac{\mu}{\eta}}, \quad (18)$$

where κ represents the bulk modulus. In the incompressible case, the bulk modulus κ of the material (and hence also the compliance $\tilde{\lambda}$) approaches infinity whereas the dilatation $\tilde{\chi}_l$ goes to zero. Hence, the product $\tilde{\lambda}\tilde{\chi}_l$ in Eq. (13), which has the meaning of a mean normal stress (Wu and Peltier, 1982), remains finite for incompressible bodies.

The relevant equations of motion for an incompressible viscoelastic body – i.e. conservation of linear momentum and Poisson's equation involving the perturbed gravitational potential – can be written as a set of six coupled first-order differential equations in terms of the radial functions (Sabadini and Vermeersen, 2004):

$$\frac{d\tilde{y}_1}{dr} - \frac{2}{r}\tilde{y}_1 + \frac{l(l+1)}{r}\tilde{y}_2, \quad (19)$$

$$\frac{d\tilde{y}_2}{dr} = -\frac{1}{r}\tilde{y}_1 + \frac{1}{r}\tilde{y}_2 + \frac{1}{\tilde{\mu}}\tilde{y}_4, \quad (20)$$

$$\frac{d\tilde{y}_3}{dr} = \frac{4}{r} \left(\frac{3\tilde{\mu}}{r} - \rho_0 g \right) \tilde{y}_1 - \frac{l(l+1)}{r} \left(\frac{6\tilde{\mu}}{r} - \rho_0 g \right) \tilde{y}_2 + \frac{l(l+1)}{r} \tilde{y}_4 - \frac{\rho_0(l+1)}{r} \tilde{y}_5 + \rho_0 \tilde{y}_6, \quad (21)$$

$$\frac{d\tilde{y}_4}{dr} = -\frac{1}{r} \left(\frac{6\tilde{\mu}}{r} - \rho_0 g \right) \tilde{y}_1 + \frac{2(2l^2 + 2l - 1)}{r^2} \tilde{\mu} \tilde{y}_2 - \frac{1}{r} \tilde{y}_3 - \frac{3}{r} \tilde{y}_4 + \frac{\rho_0}{r} \tilde{y}_5, \quad (22)$$

$$\frac{d\tilde{y}_5}{dr} = -4\pi G \rho_0 \tilde{y}_1 - \frac{l+1}{r} \tilde{y}_5 + \tilde{y}_6, \quad (23)$$

$$\frac{d\tilde{y}_6}{dr} = -\frac{4\pi G \rho_0(l+1)}{r} \tilde{y}_1 + \frac{4\pi G \rho_0 l(l+1)}{r} \tilde{y}_2 + \frac{l-1}{r} \tilde{y}_6, \quad (24)$$

where $g = 4\pi G \rho_0 r/3$ is the gravity.

In difference with previous research (e.g. Moore and Schubert, 2000; Harada and Kurita, 2006; Wahr et al., 2009), we solve this system of differential equations in the Laplace domain using the propagator matrix technique. This is an almost completely analytical way to compute the response of a layered incompressible planetary body to forces acting on it. A detailed discussion about this method is given in Sabadini and Vermeersen (2004) and will therefore not be presented in this paper.

4.2. The impulse response of interior models with a global subsurface ocean

The classical propagator matrix method inherently implies propagation of the radial functions \tilde{y}_1 to \tilde{y}_6 from the core–mantle boundary (CMB) to the surface through exclusively viscoelastic material layers. However, as suggested in Section 3, our models of Europa's interior include a material layer with zero rigidity between two viscoelastic layers: the subsurface ocean. The presence of a liquid ocean between the mantle and the ice shell changes the dynamics of the interior's response as fluid layers are not able to propagate mechanical quantities, such as deformations and stresses, from the top of the silicate mantle to the base of the ice shell. Therefore, the response of the ice shell is mechanically decoupled from the response of the silicate mantle, although remaining gravitationally coupled.

The presence of a liquid inviscid ocean in the interior of Europa introduces a challenge to the application of the propagator matrix method. As can be observed from Eq. (20), an internal fluid material layer (with $\tilde{\mu} = 0$) would cause a singularity in the radial propagation of the tangential displacement \tilde{y}_2 . This singularity degenerates the propagation of the remaining mechanical quantities (\tilde{y}_1, \tilde{y}_3 and \tilde{y}_4) and the potential stress \tilde{y}_6 through the liquid ocean. In order to circumvent this problem, we assume that Europa's subsurface ocean is in a state of hydrostatic equilibrium in both the undeformed and deformed cases and that the deformations of the fluid follow equipotential surfaces (based on Chinnery (1975)). In this way, the physical behavior of Europa's putative subsurface ocean is fully determined by Poisson's equation. If we further assume that Europa's ocean is incompressible and non-stratified, Poisson's equation reduces to Laplace's equation because $\tilde{\gamma}_l$ and $\frac{\partial \tilde{\phi}_l}{\partial r}$ become equal to zero. Then, the relevant set of differential equations can be written as

$$\frac{d\tilde{y}_5}{dr} = \tilde{y}_7, \quad (25)$$

$$\frac{d\tilde{y}_7}{dr} = \frac{l(l+1)}{r^2} \tilde{y}_5 - \frac{2}{r} \tilde{y}_7, \quad (26)$$

where the auxiliary radial function \tilde{y}_7 is simply defined as the negative of the radial derivative of the perturbed potential, i.e.

$$\tilde{y}_7 = -\frac{\partial \tilde{\Phi}_l}{\partial r} = \tilde{Q}_l^*, \quad (27)$$

or, alternatively, in terms of the potential stress \tilde{Q}_l

$$\tilde{y}_7 = \tilde{Q}_l + \frac{l+1}{r} \tilde{\Phi}_l - 4\pi G \rho_0 \tilde{U}_l = \tilde{Q}_l^*. \quad (28)$$

The same equations would hold if the subsurface ocean would be stratified in several layers with different densities. Since the density is defined as being constant within a fluid layer, the difference between Poisson's and Laplace's equations can be introduced at the boundary between the two fluid layers, i.e.

$$\tilde{Q}_l^{*(i)} = \tilde{Q}_l^{*(i+1)} + 4\pi G (\rho_0^{(i+1)} - \rho_0^{(i)}) \frac{\Phi_l^{(i+1)}}{g(r_{i+1})}, \quad (29)$$

where i is a fluid layer overlying fluid layer $i+1$ and r is the outer radius of a given fluid layer. Eq. (29) also takes into account that the radial deformation of fluid layers follows the shape of an equipotential surface.

The introduction of a subsurface ocean decouples the propagation of the tidal response from the core–mantle boundary to the surface in three parts: propagation through the mantle, propagation through the ocean and propagation through the ice shell. The first and last propagation steps obey the equations of motion for viscoelastic bodies (Eqs. (19)–(24)), while the second propagation obeys the equations of motion for fluid layers (Eqs. (25) and (26)). In order to couple the three parts of the propagation, we need to provide a set of boundary conditions at the interfaces between the ocean and both the underlying silicate mantle and the overlying ice shell. Then, the general structure of the adapted propagator matrix method becomes:

- The solution vector at the core–mantle boundary (CMB) is propagated through the silicate mantle by means of the viscoelastic propagator matrix (Sabadini and Vermeersen, 2004).
- At the mantle–ocean interface, a set of boundary conditions relates the solution vector at the top of the silicate mantle to the solution vector at the bottom of the ocean.
- The solution vector at the bottom of the ocean is propagated through the liquid ocean by means of the fluid propagator matrix.
- At the ocean–ice interface, we again link the solution vector at the top of the ocean to the solution vector at the bottom of the ice shell by a set of boundary conditions.
- The solution vector at the base of the ice shell can be further propagated up to the surface by means of the viscoelastic propagator matrix.

A detailed description of the developed methodology is presented in Appendix A.

Application of the adapted propagator matrix technique to Europa leads to the determination of the unit impulse response $\tilde{\mathbf{X}}_l(s)$ of Europa's interior to tidal forces. The unit impulse response of a planetary body, which is formally defined as the response of the body to a unit impulse excitation applied at $t = 0$, depends only on the structural and rheological properties of the interior. The actual tidal response of Europa follows from the product between the calculated unit impulse response $\tilde{\mathbf{X}}_l(s)$ and the acting tidal potential $\tilde{\Phi}_T(s)$; both expressed in the Laplace domain according to the correspondence principle. The equivalent response in the time domain can then be determined by applying the inverse Laplace transform to the outcome of the aforementioned product.

As can be observed from Eqs. (2) and (A.24), both the unit impulse response and the tidal potential are expanded in spherical harmonics. However, as can be seen from Eq. (2), the tidal potential acting on Europa is completely defined by its second harmonic degree. Therefore, we only need the second-degree term of the unit impulse response expansion in order to determine the tidal response of Europa at its surface. This term, i.e. $\tilde{\mathbf{X}}_2(s)$, follows directly from Eq. (A.24):

$$\tilde{\mathbf{X}}_2(s) = \begin{pmatrix} \tilde{U}_2(R, s) \\ \tilde{V}_2(R, s) \\ -\tilde{\Phi}_2(R, s) \end{pmatrix} = \mathbf{K}_2^e(R) + \sum_{j=1}^M \frac{\mathbf{K}_2^j(R)}{s - s_j}, \quad (30)$$

where R is the mean radius of Europa, s is the Laplace variable and $j = 1, 2, \dots, M$ are the M relaxation modes of Europa's interior and surface. Each of these relaxation modes is characterized by an inverse relaxation time s_j , which can be found by computing the non-zero roots of Eq. (A.16). The elastic limit parameter $\mathbf{K}_2^e(R)$ and

the vector residues $\mathbf{K}_2^j(R)$ are mathematically defined by Eqs. (A.25) and (A.26), respectively.

4.3. Love numbers

The response of a planetary body to the acting tidal forces is usually expressed in terms of the dimensionless tidal Love numbers h_2 , l_2 and k_2 , where h_2 and l_2 refer to the experienced radial and lateral deformations and k_2 refers to the gravitational perturbation induced by the reshaping of the planet. In the Laplace domain, the Love numbers $\tilde{h}_2(s)$ and $\tilde{l}_2(s)$ are defined as (e.g. Sabadini and Vermeersen, 2004)

$$\frac{\tilde{h}_2}{g_0} = \left(\mathbf{K}_2^e(R) + \sum_{j=1}^M \frac{\mathbf{K}_2^j(R)}{s - s_j} \right)_1, \quad (31)$$

$$\frac{\tilde{l}_2}{g_0} = \left(\mathbf{K}_2^e(R) + \sum_{j=1}^M \frac{\mathbf{K}_2^j(R)}{s - s_j} \right)_2, \quad (32)$$

where g_0 is the gravity at the surface and the subscripts 1 and 2 refer to the first and second element of the unit impulse response vector $\tilde{\mathbf{X}}_2(s)$.

As can be observed from Eqs. (31) and (32), the level of importance of viscoelasticity on the tidal response of Europa depends largely on the value of the Laplace parameter s relative to the inverse relaxation times s_j . In the elastic limit, i.e. $s \rightarrow \infty$ or when $s \gg |s_j|$, the set of Love numbers reduces to

$$\frac{h_2^e}{g_0} = (\mathbf{K}_2^e(R))_1, \quad (33)$$

$$\frac{l_2^e}{g_0} = (\mathbf{K}_2^e(R))_2, \quad (34)$$

where the constants h_2^e and l_2^e are the elastic Love numbers. These Love numbers denote the purely elastic tidal response at the surface.

On the other hand, a planetary body behaves as a fluid when s approaches zero or when $s \ll |s_j|$. In this particular case, the set of Love numbers given by Eqs. (31) and (32) reduces to

$$\frac{h_2^f}{g_0} = \frac{h_2^e}{g_0} + \sum_{j=1}^M \frac{h_{2j}^v}{g_0}, \quad (35)$$

$$\frac{l_2^f}{g_0} = \frac{l_2^e}{g_0} + \sum_{j=1}^M \frac{l_{2j}^v}{g_0}, \quad (36)$$

where the constants h_2^f and l_2^f are the so-called fluid Love numbers, and the constants h_{2j}^v and l_{2j}^v are a concise way to represent the modal strengths. The modal strengths are usually defined as

$$\frac{h_{2j}^v}{g_0} = \left(\frac{\mathbf{K}_2^j(R)}{-s_j} \right)_1, \quad (37)$$

$$\frac{l_{2j}^v}{g_0} = \left(\frac{\mathbf{K}_2^j(R)}{-s_j} \right)_2. \quad (38)$$

In contrast to the viscoelastic Love numbers \tilde{h}_2 and \tilde{l}_2 , the elastic Love numbers (h_2^e and l_2^e), fluid Love numbers (h_2^f and l_2^f) and modal strengths (h_{2j}^v and l_{2j}^v) do not depend on the Laplace parameter s .

5. Stresses at the surface of Europa

5.1. Diurnal stresses at the surface

In this research, we develop a method to derive the diurnal stress field at Europa's surface from the tidal viscoelastic response given by Eq. (30). This method is broadly similar to the one by Wahr et al. (2009), however some important differences arise from

the way both methods calculate the tidal Love numbers. Due to the subdivision of the non-elastic response into several relaxation modes, our method enables us to get a deeper insight into the physics of relaxation by studying the contribution of each relaxation mode to the tidal response. In addition, our method remains stable in the fluid limit. This allows us to determine the tidal response and subsequent stresses of interior models containing viscoelastic layers with a very small Maxwell time (i.e. low viscosity and low rigidity). The stress is defined as

$$\sigma_{ij} = \mathcal{L}^{-1}(\tilde{\Pi} \delta_{ij} + 2\tilde{\mu}(s) \tilde{\epsilon}_{ij}(s)), \quad (39)$$

where δ_{ij} is the Kronecker delta, \mathcal{L}^{-1} is the inverse Laplace transform, $\tilde{\epsilon}_{ij}(s)$ is the strain tensor and $\tilde{\Pi}$ is the product between the compliance $\tilde{\lambda}(s)$ and the dilatation $\nabla \cdot \tilde{\mathbf{u}}$. The strain tensor $\tilde{\epsilon}_{ij}(s)$ at the surface is related to the tidal response through the strain-displacement relations:

$$\tilde{\epsilon}_{rr} = \frac{1}{g_0} \frac{\partial}{\partial r} (\tilde{h}_2(R, s) \tilde{\Phi}_T), \quad (40)$$

$$\tilde{\epsilon}_{r\theta} = 0, \quad (41)$$

$$\tilde{\epsilon}_{r\phi} = 0, \quad (42)$$

$$\tilde{\epsilon}_{\theta\theta} = \frac{1}{rg_0} \left(\tilde{l}_2(R, s) \frac{\partial^2 \tilde{\Phi}_T}{\partial \theta^2} + \tilde{h}_2(R, s) \tilde{\Phi}_T \right), \quad (43)$$

$$\tilde{\epsilon}_{\phi\phi} = \frac{1}{rg_0} \left([\tilde{h}_2(R, s) - 6\tilde{l}_2(R, s)] \tilde{\Phi}_T - \tilde{l}_2(R, s) \frac{\partial^2 \tilde{\Phi}_T}{\partial \theta^2} \right), \quad (44)$$

$$\tilde{\epsilon}_{\theta\phi} = \frac{1}{rg_0} \tilde{l}_2(R, s) \left(\frac{1}{\sin \theta} \frac{\partial^2 \tilde{\Phi}_T}{\partial \theta \partial \phi} - \frac{\cos \theta}{\sin^2 \theta} \frac{\partial \tilde{\Phi}_T}{\partial \phi} \right), \quad (45)$$

where the Laplace-transform of the diurnal tidal potential at the surface ($\tilde{\Phi}_T$) is a function of s , θ and ϕ , i.e. $\tilde{\Phi}_T = \tilde{\Phi}_T(R, s, \theta, \phi)$. The diurnal tidal potential is defined by the terms $\tilde{\Phi}_T^{e1}$, $\tilde{\Phi}_T^{e2}$ and $\tilde{\Phi}_T^{o1}$ in Eq. (2).

Furthermore, the mean normal stress $\tilde{\Pi} = \sum_{l=0}^{\infty} \tilde{\lambda}_l Y_l(\theta, \phi)$ is related to the tidal response by the surface boundary condition regarding the radial stress (i.e. $\tilde{\sigma}_{rr}(R, s) = 0$). Based on Eqs. (13) and (19), we can write:

$$\tilde{\Pi} = \frac{2\tilde{\mu}(s)}{rg_0} (2\tilde{h}_2(R, s) - 6\tilde{l}_2(R, s)) \tilde{\Phi}_T. \quad (46)$$

The non-zero elements of the stress tensor acting on the surface of an incompressible Maxwell body can then be retrieved by substituting Eqs. (40)–(46) into Eq. (39), i.e.:

$$\sigma_{\theta\theta} = \mathcal{L}^{-1} \left(2\tilde{\mu}(s) \cdot \frac{1}{rg_0} \left\{ \tilde{l}_2(R, s) \frac{\partial^2 \tilde{\Phi}_T}{\partial \theta^2} + 3(\tilde{h}_2(R, s) - 2\tilde{l}_2(R, s)) \tilde{\Phi}_T \right\} \right), \quad (47)$$

$$\sigma_{\phi\phi} = \mathcal{L}^{-1} \left(2\tilde{\mu}(s) \cdot \frac{1}{rg_0} \left\{ 3(\tilde{h}_2(R, s) - 4\tilde{l}_2(R, s)) \tilde{\Phi}_T - \tilde{l}_2(R, s) \frac{\partial^2 \tilde{\Phi}_T}{\partial \theta^2} \right\} \right), \quad (48)$$

$$\sigma_{\theta\phi} = \mathcal{L}^{-1} \left(2\tilde{\mu}(s) \cdot \frac{\tilde{l}_2(R, s)}{rg_0} \left\{ \frac{1}{\sin \theta} \frac{\partial^2 \tilde{\Phi}_T}{\partial \theta \partial \phi} - \frac{\cos \theta}{\sin^2 \theta} \frac{\partial \tilde{\Phi}_T}{\partial \phi} \right\} \right). \quad (49)$$

Eqs. (47)–(49) show that viscoelasticity influences the state of stresses at the surface in two ways: (1) through the compliance $\tilde{\mu}(s)$, which is related to the rheological properties of the

lithosphere, and (2) by the viscoelastic response itself, which is represented by the Love numbers $\tilde{h}_2(R, s)$ and $\tilde{l}_2(R, s)$. We redefine the compliance $\tilde{\mu}(s)$ as

$$\tilde{\mu}(s) = \mu - \frac{\mu \cdot \frac{\mu}{\eta}}{s + \frac{\mu}{\eta}} = \mu \left(1 - \frac{1}{1 + s\tau_M} \right) = \mu(1 - v(s, \tau_M)), \quad (50)$$

where $\tau_M = \eta/\mu$ is defined as the characteristic Maxwell time of the lithosphere. This parameter gives an indication of the time scale at which the rheological behavior of a material shows a transition from elastic to viscous. The term $v(s, \tau_M)$ represents the relaxation of the elastic shear modulus as a function of s and the Maxwell time τ_M . A close inspection of Eq. (50) shows that relaxation becomes more important for time scales much larger than the characteristic Maxwell time (i.e. $s \ll 1/\tau_M$). Based on these definitions, we can also refer to the compliance $\tilde{\mu}(s)$ as the effective shear modulus of the lithosphere.

Explicit analytical expressions for the diurnal stresses $\sigma_{\theta\theta}$, $\sigma_{\phi\phi}$ and $\sigma_{\theta\phi}$ can be derived by substituting the Laplace transform of Eq. (2) (only the diurnal terms Φ_T^{e1} , Φ_T^{e2} and Φ_T^{o1} , Eqs. (31)–(38) and (50) into Eqs. (47)–(49). After some analytical manipulation, we obtain

$$\sigma_{\theta\theta} = \sigma_{\theta\theta}^e + \sigma_{\theta\theta}^v, \quad (51)$$

$$\sigma_{\phi\phi} = \sigma_{\phi\phi}^e + \sigma_{\phi\phi}^v, \quad (52)$$

$$\sigma_{\theta\phi} = \sigma_{\theta\phi}^e + \sigma_{\theta\phi}^v, \quad (53)$$

where the contribution of the elastic response (superscript e) and relaxation modes (superscript v) to the diurnal stress tensor are given by

$$\begin{aligned} \sigma_{\theta\theta}^e = \frac{1}{2} \frac{n^2 R \mu}{g_0} \frac{1}{\sqrt{1 + \mathcal{A}^2}} & \left\{ -6e\beta_{2,0}^{\theta\theta}(\theta) \cos(nt + \arctan(\mathcal{A})) \right. \\ & + e\beta_{2,2}^{\theta\theta}(\theta) [4 \sin(2\phi) \sin(nt + \arctan(\mathcal{A})) \\ & + 3 \cos(2\phi) \cos(nt + \arctan(\mathcal{A}))] \\ & \left. + 4 \cos(\varepsilon) \sin(\varepsilon) \beta_{2,1}^{\theta\theta}(\theta) [\cos(\phi) \sin(\omega + nt + \arctan(\mathcal{A}))] \right\}, \end{aligned} \quad (54)$$

$$\begin{aligned} \sigma_{\theta\theta}^v = \frac{1}{2} \frac{n^2 R \mu}{g_0} \frac{1}{\sqrt{1 + \mathcal{A}^2}} \sum_{j=1}^M & \left(\frac{1}{\sqrt{1 + \Gamma_j^2}} \right. \\ & \times \left\{ -6e\beta_{2,0}^{\theta\theta j}(\theta) \cos(nt - \arctan(\Gamma_j) + \arctan(\mathcal{A})) \right. \\ & + 4e\beta_{2,2}^{\theta\theta j}(\theta) \sin(2\phi) \sin(nt - \arctan(\Gamma_j) + \arctan(\mathcal{A})) \\ & + 3e\beta_{2,2}^{\theta\theta j}(\theta) \cos(2\phi) \cos(nt - \arctan(\Gamma_j) + \arctan(\mathcal{A})) \\ & + 4 \cos(\varepsilon) \sin(\varepsilon) \beta_{2,1}^{\theta\theta j}(\theta) \\ & \left. \times [\cos(\phi) \sin(\omega + nt - \arctan(\Gamma_j) + \arctan(\mathcal{A}))] \right\} \Bigg), \end{aligned} \quad (55)$$

$$\begin{aligned} \sigma_{\phi\phi}^e = \frac{1}{2} \frac{n^2 R \mu}{g_0} \frac{1}{\sqrt{1 + \mathcal{A}^2}} & \left\{ -6e\beta_{2,0}^{\phi\phi}(\theta) \cos(nt + \arctan(\mathcal{A})) \right. \\ & + e\beta_{2,2}^{\phi\phi}(\theta) [4 \sin(2\phi) \sin(nt + \arctan(\mathcal{A})) \\ & + 3 \cos(2\phi) \cos(nt + \arctan(\mathcal{A}))] \\ & \left. + 4 \cos(\varepsilon) \sin(\varepsilon) \beta_{2,1}^{\phi\phi}(\theta) [\cos(\phi) \sin(\omega + nt + \arctan(\mathcal{A}))] \right\}, \end{aligned} \quad (56)$$

$$\begin{aligned} \sigma_{\phi\phi}^v = \frac{1}{2} \frac{n^2 R \mu}{g_0} \frac{1}{\sqrt{1 + \mathcal{A}^2}} \sum_{j=1}^M & \left(\frac{1}{\sqrt{1 + \Gamma_j^2}} \right. \\ & \times \left\{ -6e\beta_{2,0}^{\phi\phi j}(\theta) \cos(nt - \arctan(\Gamma_j) + \arctan(\mathcal{A})) \right. \\ & + 4e\beta_{2,2}^{\phi\phi j}(\theta) \sin(2\phi) \sin(nt - \arctan(\Gamma_j) + \arctan(\mathcal{A})) \\ & + 3e\beta_{2,2}^{\phi\phi j}(\theta) \cos(2\phi) \cos(nt - \arctan(\Gamma_j) + \arctan(\mathcal{A})) \\ & + 4 \cos(\varepsilon) \sin(\varepsilon) \beta_{2,1}^{\phi\phi j}(\theta) \\ & \left. \times [\cos(\phi) \sin(\omega + nt - \arctan(\Gamma_j) + \arctan(\mathcal{A}))] \right\} \Bigg), \end{aligned} \quad (57)$$

$$\begin{aligned} \sigma_{\theta\phi}^e = \frac{1}{2} \frac{n^2 R \mu}{g_0} \frac{1}{\sqrt{1 + \mathcal{A}^2}} & \times \left\{ 2e\beta_{2,2}^{\theta\phi}(\theta) [4 \cos(2\phi) \sin(nt + \arctan(\mathcal{A})) \right. \\ & - 3 \sin(2\phi) \cos(nt + \arctan(\mathcal{A}))] \\ & \left. + 4 \cos(\varepsilon) \sin(\varepsilon) \beta_{2,1}^{\theta\phi}(\theta) \times [\sin(\phi) \sin(\omega + nt + \arctan(\mathcal{A}))] \right\}, \end{aligned} \quad (58)$$

$$\begin{aligned} \sigma_{\theta\phi}^v = \frac{1}{2} \frac{n^2 R \mu}{g_0} \frac{1}{\sqrt{1 + \mathcal{A}^2}} \sum_{j=1}^M & \left(\frac{1}{\sqrt{1 + \Gamma_j^2}} \right. \\ & \times \left\{ 8e\beta_{2,2}^{\theta\phi j}(\theta) \cos(2\phi) \sin(nt - \arctan(\Gamma_j) + \arctan(\mathcal{A})) \right. \\ & - 6e\beta_{2,2}^{\theta\phi j}(\theta) \sin(2\phi) \cos(nt - \arctan(\Gamma_j) + \arctan(\mathcal{A})) \\ & + 4 \cos(\varepsilon) \sin(\varepsilon) \beta_{2,1}^{\theta\phi j}(\theta) \\ & \left. \times [\sin(\phi) \sin(\omega + nt - \arctan(\Gamma_j) + \arctan(\mathcal{A}))] \right\} \Bigg), \end{aligned} \quad (59)$$

where the Beta-functions depend on the elastic Love numbers h_2^e and l_2^e , the modal strengths $h_{2,j}^v$ and $l_{2,j}^v$, and the co-latitude θ . These functions are listed in Appendix C. The dimensionless ratios \mathcal{A} and Γ_j are defined as

$$\mathcal{A} = \frac{\mu/\eta}{n} = \frac{T}{2\pi\tau_M}, \quad (60)$$

and

$$\Gamma_j = \frac{n}{-s_j} = \frac{2\pi\tau_j}{T}, \quad (61)$$

where n is the mean angular velocity of Europa's orbit, T is the orbital period, $-s_j$ is the inverse relaxation time of the mode j , and $\tau_j = -1/s_j$ is the corresponding relaxation time.

From a theoretical point of view, the dimensionless ratio \mathcal{A} describes the relaxation state of diurnal stresses at Europa's surface. As can be observed from Fig. 1, relaxation at the surface starts to become important for values of \mathcal{A} larger than 0.1. In the case of Europa's lithosphere, $\mathcal{A} > 0.1$ would correspond to viscosities smaller than 1.7×10^{15} Pa s for a rigidity $\mu = 3.487$ GPa, or to viscosities smaller than 4.9×10^{14} Pa s for a rigidity $\mu = 1$ GPa. Such low viscosities are, however, more representative for the lower portion of the icy shell and are several orders of magnitude smaller than the plausible values for the viscosity of a cold, conducting lithosphere (Husmann et al., 2002; Nimmo and Manga, 2009). For this reason, we can state that diurnal stresses are elastically stored in the lithosphere due to the high viscosity of the upper ice layer and/or the high frequency of the forcing function. This statement is in agreement with (Wahr et al., 2009).

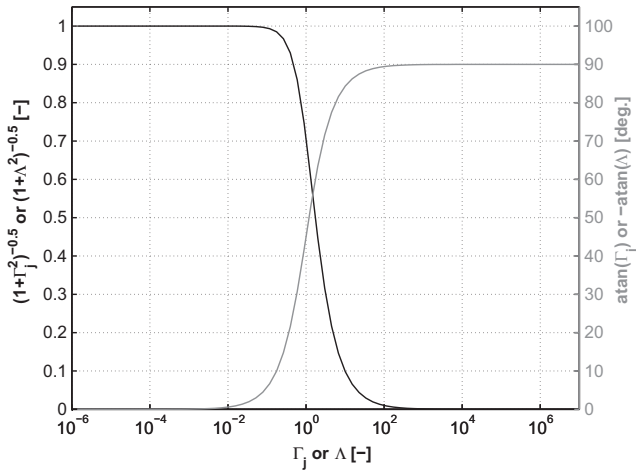


Fig. 1. Theoretical effect of the ratio $\Gamma_j = \frac{\eta}{\mu}$ on the contribution of a relaxation mode j to the surface diurnal stress at the surface, and effect of the ratio $\Lambda = \frac{\mu}{\eta}$ on the relaxation state of diurnal stresses at the surface. Regarding the ratio Γ_j , the dark curve represents the attenuation of the corresponding modal strength h_{2j}^v (1 is no attenuation and 0 is complete attenuation) and the light curve shows the phase-lag of the contribution of mode j to the diurnal stress. Regarding the ratio Λ , the dark curve presents the importance of viscous relaxation on the magnitude of diurnal stresses at the surface (1 means that stresses are elastically stored, whereas 0 means complete relaxation of the stresses) and the light curve gives the phase-lag caused by relaxation.

On the other hand, viscoelasticity could have an important effect on the magnitude and geographical distribution of surface diurnal stresses. As shown by Eqs. (55), (57) and (59), every relaxation mode j contributes in a non-elastic way to the surface diurnal stress. However, not all modal contributions are large enough to induce an observable viscoelastic effect on the diurnal stress field. Fig. 1 depicts a graphical representation of the influence of the ratio Γ_j on the contribution of a relaxation mode j to the surface diurnal stress. The dark curve in Fig. 1 gives the effect of Γ_j on the modal strengths (h_{2j}^v and l_{2j}^v), and hence on the magnitude of the viscoelastic contribution to the surface diurnal stress. We observe that the contribution of relaxation modes with Γ_j larger than 100 (i.e. τ_j larger than 52.5 days in Europa's case) can be safely neglected, as their corresponding modal strengths are reduced by more than two orders of magnitude. Therefore, the slow-relaxing modes C_0 , M_3 , M_2 and M_0 (see the numerical values presented in Table 3 for an example) will not have an influence on diurnal stresses. Only the fast-relaxing transient modes T_1 and T_2 remain as potential candidates, with T_2 as the most influential mode due to its larger modal strengths and its faster relaxation time. In addition, Γ_j introduces a phase delay in the tidal response which generates a westward shift of the stress patterns at the surface. The light curve in Fig. 1 shows that relaxation modes with a very short relaxation time ($\Gamma_j < 0.01$ or $\tau_j < 8$ min in Europa's case) contribute in an effectively elastic way to the surface diurnal stress, as their corresponding phase-lag becomes negligibly small. The phase-lag increases significantly for larger relaxation times, becoming 5.82°

Table 3
Tidal response of the reference model of Europa's interior to diurnal tidal forces.

Mode	τ_j (s)	Γ_j (-)	h_{2j}^e or h_{2j}^v (-)	l_{2j}^e or l_{2j}^v (-)
Elastic	–	–	1.15100×10^0	3.07996×10^{-1}
C_0	7.02026×10^{10}	1.43745×10^6	5.17509×10^{-2}	1.40296×10^{-2}
M_3	9.15741×10^9	1.87504×10^5	7.16925×10^{-1}	1.94722×10^{-1}
M_2	9.75577×10^{10}	1.99756×10^6	1.38050×10^{-3}	2.35200×10^{-4}
M_0	2.91957×10^{11}	5.97802×10^6	3.69559×10^{-2}	1.00498×10^{-2}
T_1	1.73366×10^5	3.54978×10^0	7.19132×10^{-5}	6.00107×10^{-3}
T_2	3.07948×10^4	6.30543×10^{-1}	8.49611×10^{-2}	2.26471×10^{-2}

for $\Gamma_j = 0.1$, 45° for $\Gamma_j = 1$ and 84.3° for $\Gamma_j = 10$. Since the ratio Γ_j has opposite effects on the magnitude and phase-lag (Fig. 1), the viscoelastic effect on surface diurnal stresses will be largest for strong modes with $\Gamma_j \sim 1$. In our modeling, the relaxation time of the strong transient mode T_2 satisfies the condition $\Gamma_j \sim 1$ only if the viscosity of the asthenosphere ranges between 1.0×10^{14} Pa s and 1.0×10^{15} Pa s. These are typical values for the viscosity of a high-dissipative and convective asthenosphere, hence viscoelastic effects on Europa's diurnal stress field are plausible. The effect of viscoelasticity is enhanced by thick ice layers and high values for the rigidity of ice, as both parameters lead to an increase of the modal strengths. Although not directly relevant to Europa, viscoelastic effects on the diurnal stress field become dominant for oceanless models with an extremely low-viscous asthenosphere (less than 1.0×10^{13} Pa s). In these cases, the diurnal stress field at the surface will be considerably different than in all cases with a subsurface ocean.

5.2. NSR stresses at the surface

Based on the interpretation of tectonic features, non-synchronous rotation (NSR) of Europa's ice shell has been widely suggested as an important mechanism to generate large stresses (\sim MPa) on the surface (Leith and McKinnon, 1996; Greenberg et al., 1998; Gleeson et al., 2005; Harada and Kurita, 2007; Hurford et al., 2007; Kattenhorn and Hurford, 2009; Sotin et al., 2009; Wahr et al., 2009). From a dynamical perspective, NSR would take place if tidal torques acting on the decoupled shell would drive the rotation of the shell to a slightly faster than synchronous state (Greenberg and Weidenschilling, 1984). However, as shown by Bills et al. (2009), the tidal torque acting on Europa cannot be large enough to overcome the counteracting gravitational torque exerted by Jupiter on permanent asymmetries in the figure of Europa (represented by the difference between the equatorial moments of inertia, i.e. $B - A$). In addition, recent research by Goldreich and Mitchell (2010) points out that the tidal torque is counteracted by an elastic torque resulting from rotation of the shell with respect to the equilibrium figure of the ocean. Despite the occurrence of NSR cannot be precluded from this study, the resulting stresses on the surface would be too small to create a crack (Goldreich and Mitchell, 2010). Although non-synchronous rotation (NSR) of Europa's ice shell is strongly opposed by the dynamical considerations discussed above, NSR is still possible if driven by mass displacements in the interior of the body (Ojakangas and Stevenson, 1989b; Bills et al., 2009).

In this paper, we compute the NSR stress field at Europa's surface from the Maxwell viscoelastic response (Eq. (30)) and the NSR forcing function (term Φ_T^{ns} in Eq. (2)) by applying the methodology introduced in Section 5.1. As a result, we are allowed to write each non-zero element of the NSR stress tensor in the form given by Eqs. (47)–(49). Before using these equations to compute NSR

Table 4
Tidal response of the reference model of Europa's interior to NSR forces.

Mode ^a	τ_j (year)	γ_j^b (-)	h_{2j}^e or h_{2j}^v (-)	l_{2j}^e or l_{2j}^v (-)
Elastic	–	–	1.85155×10^0	4.95366×10^{-1}
M_2	9.24992×10^3	9.68650×10^0	3.60537×10^{-2}	9.80448×10^{-3}
M_0	3.09117×10^3	3.23707×10^0	1.80231×10^{-3}	3.07295×10^{-4}
T_1	5.49324×10^{-3}	5.75251×10^{-6}	1.16432×10^{-4}	9.28203×10^{-3}
T_2	9.84029×10^{-4}	1.03047×10^{-6}	1.53522×10^{-1}	4.09211×10^{-2}

^a The core-mode C_0 and the mantle-mode M_3 vanish from the NSR response, since we assumed that the synchronously locked rocky interior behaves as a fluid with respect to NSR forces.

^b Corresponds to the minimum period of NSR, i.e. $T_{ns} = 12000$ years ($\Lambda \approx 0.1$).

surface stresses, we need to remark that the Love numbers \tilde{h}_2 and \tilde{l}_2 required for NSR calculations differ from the Love numbers used to derive the diurnal response (compare Tables 3 and 4). The different set of tidal Love numbers results from our assumption to keep the rocky interior synchronously locked while the ice shell experiences NSR. As the rocky mantle remains tidally locked, the stresses induced by the formation of the mantle's bulge had sufficient time to relax completely and, therefore, the response of the rocky interior to the NSR forcing function can be described as being purely fluid. From a modeling perspective, we can describe this physical behavior by decreasing the rigidity of the mantle μ to values relevant for near-fluid materials, i.e. $\mu \approx 0$ (see also Wahr et al., 2009). After taking these observations into account, we can proceed to express the NSR stress field at Europa's $\hat{\sigma}_{ij}$ as a combination of a purely elastic part (superscript e) and the contribution from the relaxation modes (superscript v):

$$\hat{\sigma}_{\theta\theta} = \hat{\sigma}_{\theta\theta}^e + \hat{\sigma}_{\theta\theta}^v, \quad (62)$$

$$\hat{\sigma}_{\phi\phi} = \hat{\sigma}_{\phi\phi}^e + \hat{\sigma}_{\phi\phi}^v, \quad (63)$$

$$\hat{\sigma}_{\theta\phi} = \hat{\sigma}_{\theta\phi}^e + \hat{\sigma}_{\theta\phi}^v, \quad (64)$$

where the individual stress components in Eqs. (62)–(64) are defined by

$$\hat{\sigma}_{\theta\theta}^e = \frac{1}{2} \frac{n^2 r \mu}{g_0} \frac{1}{\sqrt{\Delta^2 + 1}} \alpha_{2,2}^{\theta\theta}(\theta) \cos(2\phi + 2\Omega_{ns}t + \arctan(\Delta)), \quad (65)$$

$$\hat{\sigma}_{\theta\theta}^v = \frac{1}{2} \frac{n^2 r \mu}{g_0} \frac{1}{\sqrt{\Delta^2 + 1}} \times \sum_{j=1}^M \left\{ \frac{1}{\sqrt{1 + \gamma_j^2}} \alpha_{2,2}^{\theta\theta j}(\theta) \cos(2\phi + 2\Omega_{ns}t + \arctan(\Delta) - \arctan(\gamma_j)) \right\}, \quad (66)$$

$$\hat{\sigma}_{\phi\phi}^e = \frac{1}{2} \frac{n^2 r \mu}{g_0} \frac{1}{\sqrt{\Delta^2 + 1}} \alpha_{2,2}^{\phi\phi}(\theta) \cos(2\phi + 2\Omega_{ns}t + \arctan(\Delta)), \quad (67)$$

$$\hat{\sigma}_{\phi\phi}^v = \frac{1}{2} \frac{n^2 r \mu}{g_0} \frac{1}{\sqrt{\Delta^2 + 1}} \times \sum_{j=1}^M \left\{ \frac{1}{\sqrt{1 + \gamma_j^2}} \alpha_{2,2}^{\phi\phi j}(\theta) \cos(2\phi + 2\Omega_{ns}t + \arctan(\Delta) - \arctan(\gamma_j)) \right\}, \quad (68)$$

$$\hat{\sigma}_{\theta\phi}^e = -\frac{n^2 r \mu}{g_0} \frac{1}{\sqrt{\Delta^2 + 1}} \alpha_{2,2}^{\theta\phi}(\theta) \sin(2\phi + 2\Omega_{ns}t + \arctan(\Delta)), \quad (69)$$

$$\hat{\sigma}_{\theta\phi}^v = -\frac{n^2 r \mu}{g_0} \frac{1}{\sqrt{\Delta^2 + 1}} \times \sum_{j=1}^M \left\{ \frac{1}{\sqrt{1 + \gamma_j^2}} \alpha_{2,2}^{\theta\phi j}(\theta) \sin(2\phi + 2\Omega_{ns}t + \arctan(\Delta) - \arctan(\gamma_j)) \right\}, \quad (70)$$

where the alpha functions describe the dependence of NSR stresses on the interior's response (Love numbers) and the co-latitude (see Appendix C). Furthermore, the dimensionless ratio Δ , which describes the relaxation state of NSR stresses at Europa's surface, is defined by

$$\Delta = \frac{\mu/\eta}{2\Omega_{ns}} = \frac{T_{ns}}{4\pi\tau_M}, \quad (71)$$

and the ratio γ_j , which describes the influence of a relaxation mode to NSR stresses, is defined by

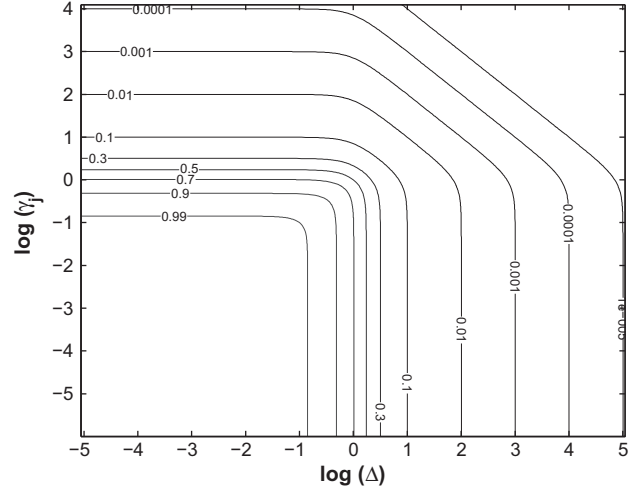


Fig. 2. Viscoelastic relaxation state of the contribution of a relaxation mode j to NSR stresses as a function of the dimensionless parameters $\Delta = \frac{\mu/\eta}{2\Omega_{ns}}$ and $\gamma_j = \frac{2\Omega_{ns}}{-s_j}$. A contour line approaching the value of 1 represents no relaxation, whereas contour lines approaching the value of 0 represent full relaxation.

$$\gamma_j = \frac{2\Omega_{ns}}{-s_j} = \frac{4\pi\tau_j}{T_{ns}}. \quad (72)$$

In Eqs. (71) and (72), the frequency of the NSR forcing function is defined as twice the constant angular rate of NSR, i.e. $2\Omega_{ns}$. This definition is motivated by the fact that a fixed point on the surface of Europa's rotating shell crosses the tidal bulge twice during one period of NSR, under the assumption that the angular rate Ω_{ns} remains constant.

The combined effect of Δ and γ_j on the various components of the NSR stress field can be analyzed with support of Figs. 2 and 3, in which the relaxation behavior of very fast relaxation modes (i.e. $\gamma_j \ll 0.1$) provides a good approximation to the behavior of the purely elastic contribution to NSR stresses. Both figures show that viscoelastic relaxation in the lithospheric shell starts to strongly influence the behavior of NSR stresses when Δ becomes larger than ~ 0.1 . However, as shown by Fig. 2, viscoelastic relaxation has a relatively larger effect on nearly-elastic contributions to NSR stresses ($\gamma_j < 0.1$) than on contributions from slow relaxation modes. This behavior is logical, as stresses related to slow relaxation

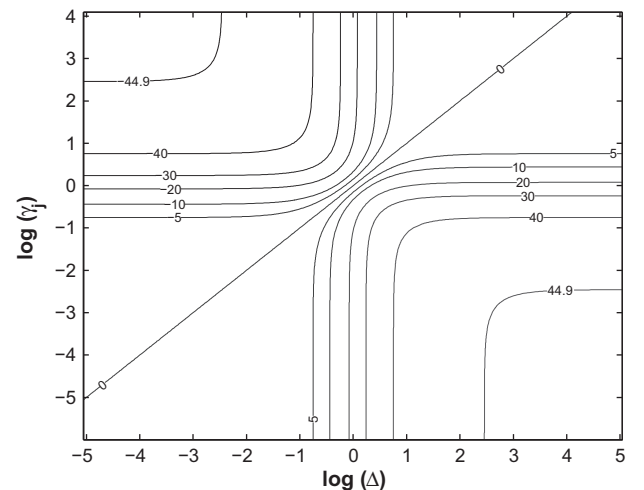


Fig. 3. Westward longitudinal shift of NSR stress patterns at the surface as a function of the dimensionless parameters $\Delta = \frac{\mu/\eta}{2\Omega_{ns}}$ and $\gamma_j = \frac{2\Omega_{ns}}{-s_j}$.

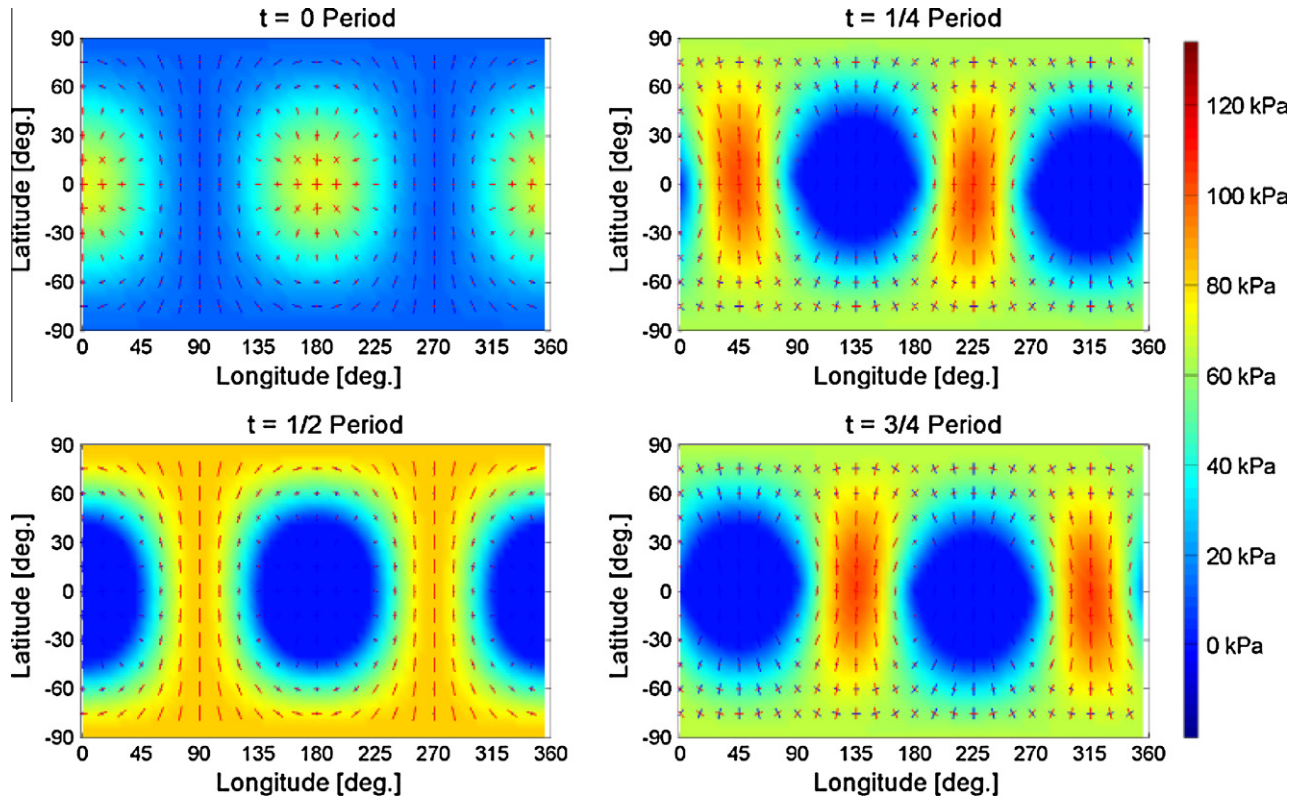


Fig. 4. Diurnal stress field at the surface of the reference model of Europa's interior (Table 2) for an eccentricity $e = 0.0094$ and an obliquity $\varepsilon = 0.1^\circ$. The stress patterns are given at four different positions on Europa's orbit around Jupiter.

modes are already attenuated by the viscoelastic character of the response itself. Besides attenuation of the magnitude, viscoelastic relaxation also introduces a westward shift on the spatial distribution of stress patterns at the surface. Fig. 3 shows that the longitudinal shift in westward direction can become as large as 45° for $\Delta > 100$ and $\gamma_j < 0.1$, i.e. in a regime where NSR stresses are being severely relaxed away.

6. Results

The diurnal and NSR stress fields acting on Europa's surface are important factors in the study of the formation and evolution of tectonic features on Europa's surface. Stress fields on planetary surfaces are commonly expressed in location-dependent coordinates defined by the so-called principal axes. These axes are aligned in such a way that the planes normal to them are not affected by shear stresses (Ranalli, 1995). The normal stresses working along the principal axes are defined as the principal stresses. The derivation of principal stresses and axes is a typical eigenvalue problem applied to the diurnal stress tensor (Eqs. (51)–(59)) and/or NSR stress tensor (Eqs. (62)–(70)), where the principal stresses are given by the eigenvalues and the principal axes by the corresponding eigenvectors. The resulting diurnal stress field acting at the surface of the reference model of Europa's interior is graphically presented in Fig. 4 at four different positions along Europa's orbit. As expected, the diurnal stress field closely follows the radial displacement field, showing tension where Europa's figure stretches (red¹ lines in Fig. 4) and compression where Europa's figure

squeezes (blue lines in Fig. 4). This result is rather expected because diurnal stresses acting on Europa's surface are always elastically stored in the lithosphere, i.e. $\Delta \ll 0.1$ (see Fig. 1).

Although the largest part of diurnal stresses is caused by the eccentricity, we cannot neglect the effect of a small non-zero obliquity. As can be observed from Fig. 4, a small obliquity of 0.1° already breaks the symmetric distribution of stress patterns with respect to the equator. This effect is enhanced for larger values for the obliquity, as is clearly shown by Fig. 5 for a hypothetical obliquity of 0.5° . The rupture of the symmetry with respect to the equator leads to latitudinal shifts of the tensile and compressive bulges, thereby yielding changes in the orientation and magnitude of the diurnal stress patterns (see Fig. 5). In our example, increasing the obliquity from 0.1° to 0.5° leads, on average, to $\sim 9\%$ larger stresses at Europa's surface, whereas the effect on the spatial distribution is clearly visible from Figs. 4 and 5. At mid-latitudes, where the influence of a non-zero obliquity is largest, diurnal stresses can locally become even twice as large after increasing the value of the obliquity from 0.1° to 0.5° .

Diurnal stresses at the surface of Europa depend on the rheological and structural properties of the interior through the tidal Love numbers h_2 and l_2 . From all physical parameters of the interior, the largest effect on the tidal response, deformations and stresses is caused by the existence or non-existence of a subsurface ocean below the ice shell. As shown by Figs. 6 and 7, diurnal stresses are often much larger (more than one order of magnitude) when a subsurface ocean is present below the ice shell. However, as shown by Fig. 6, diurnal stresses might become even larger if an extremely low-viscous asthenosphere (i.e. $\eta_{ast} = 10^{12}$ Pa s) extends down to the upper boundary of the silicate mantle. This peculiar behavior is caused by a decrease in the relaxation time of the strong transient modes T_1 and T_2 towards values comparable to the inverse of Europa's mean motion (keep in mind that the relaxation time of

¹ For interpretation of color in Figs. 4, 5, 9 and 12, the reader is referred to the web version of this article.

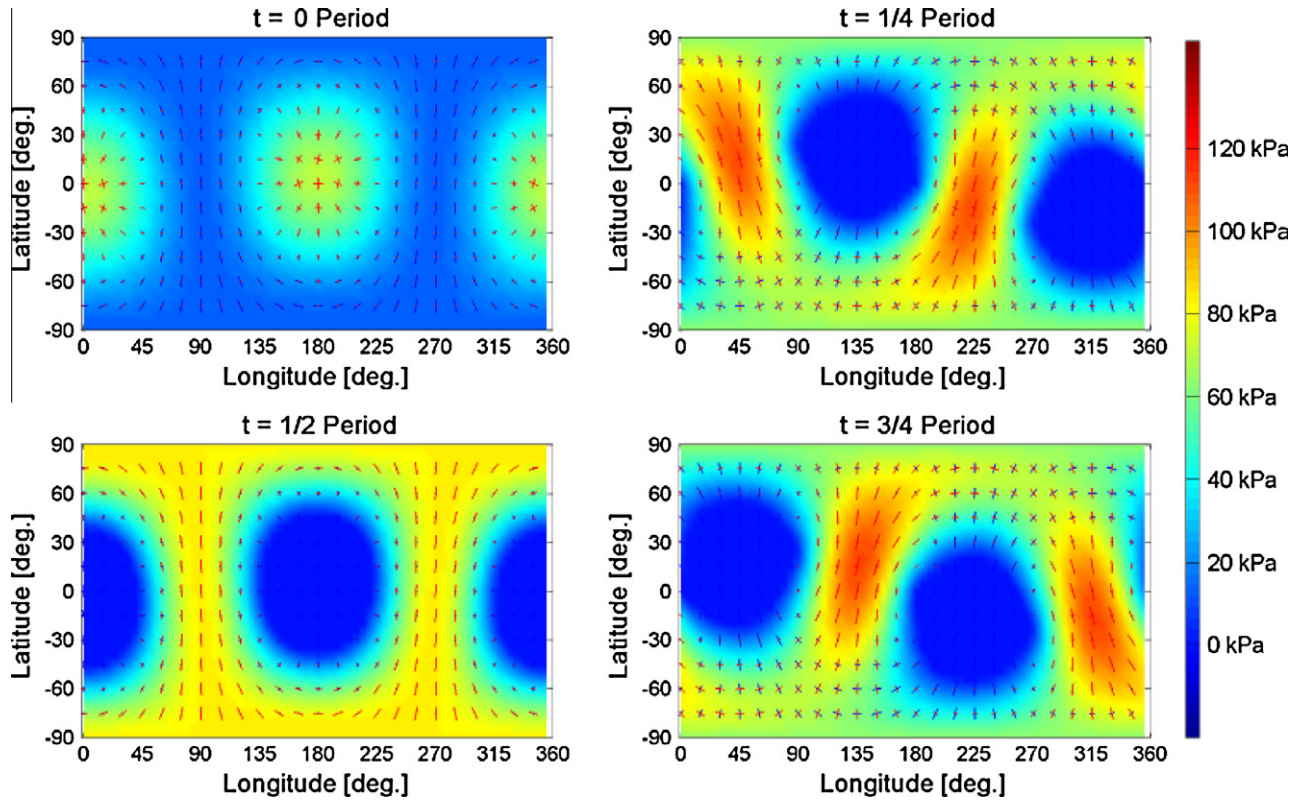


Fig. 5. Diurnal stress field at the surface of the reference model of Europa's interior (Table 2) for an eccentricity $e = 0.0094$ and an obliquity $\varepsilon = 0.5^\circ$. The stress patterns are given at four different positions on Europa's orbit around Jupiter.

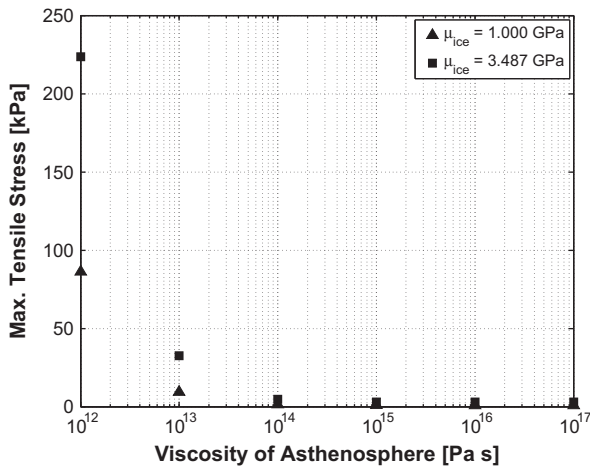


Fig. 6. Magnitude of the largest tensile stresses acting on Europa's surface as a function of the viscosity of the asthenosphere for interior models without a subsurface ocean (ice shell is 130 km thick). The squares correspond to an ice rigidity of $\mu_{ice} = 3.487$ GPa and the triangles to an ice rigidity of $\mu_{ice} = 1$ GPa. In all cases, the eccentricity is set at $e = 0.0094$ and the obliquity at $\varepsilon = 0.1^\circ$.

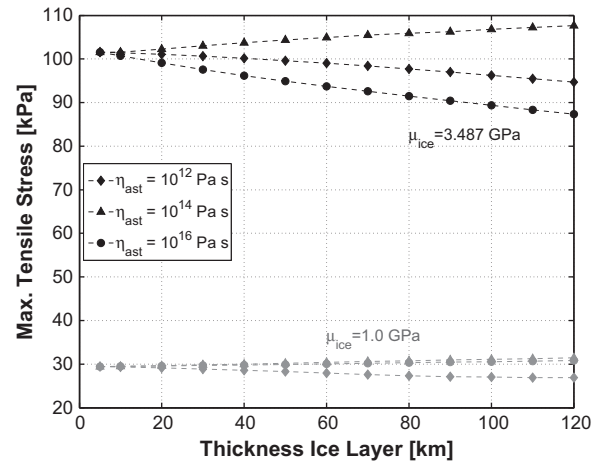


Fig. 7. Magnitude of the largest tensile stresses acting on Europa's surface as a function of the rigidity of ice, thickness of the ice shell and viscosity of the asthenosphere. The black curves correspond to an ice rigidity of $\mu_{ice} = 3.487$ GPa and the gray curves to an ice rigidity of $\mu_{ice} = 1$ GPa. In all cases, the bottom of the ocean is set at 130 km from the surface, the eccentricity at $e = 0.0094$ and the obliquity at $\varepsilon = 0.1^\circ$.

the transient modes T_1 and T_2 does not necessarily need to be comparable to the Maxwell time of the asthenosphere). Since also the modal strengths of T_1 and T_2 become larger than the elastic Love numbers, the diurnal stress field at the surface will be characterized by a large longitudinal phase shift which can exceed the 40° .

The influence of a subsurface ocean on surface diurnal stresses is by far the largest, but certainly not the only one. As shown by Fig. 7, the magnitude of surface diurnal stresses depends roughly linearly on the elastic rigidity of the lithospheric shell, especially for models with a thin ice shell (less than 10 km). However, devi-

ations from a perfect linear relation are clearly observable as the thickness of the shell increases. These deviations are caused by the combined effect of the asthenosphere's thickness and viscosity, and are enhanced at larger values for the elastic rigidity of ice-I. As shown in Fig. 7, the largest deviations from the elastic state (represented by the curves for $\eta_{ast} = 10^{16}$ Pa s) occur for values of the asthenosphere's viscosity for which the Maxwell time of this layer approaches the inverse of Europa's mean motion (i.e. between $\eta_{ast} = 10^{14}$ Pa s to $\eta_{ast} = 10^{15}$ Pa s). For extremely low values for the asthenosphere's viscosity (i.e. $\eta_{ast} = 10^{12}$ Pa s), the asthenosphere

behaves as a fluid. Hence, as can be observed from Fig. 7, the magnitude of surface diurnal stresses is nearly independent of the ice thickness.

The combined effect of the asthenosphere's viscosity and thickness also leads to a westward shift in the surface distribution of the surface stress patterns. The amount of phase shift ζ depends on the ratio Γ_j of the dominant relaxation mode T_2 , and is therefore strongest when the relaxation time of T_2 is comparable to the inverse of Europa's mean angular velocity. This effect is illustrated in Fig. 8, where we observe that phase shifts up to $\zeta = 7^\circ$ are plausible for interior models with a thick ice shell and highly dissipative asthenosphere (i.e. $\eta_{ast} = 10^{14}$ Pa s). The value of the phase shift, however, does not indicate the actual longitudinal shift of the stress patterns at Europa's surface. Instead, it denotes the time delay of the shell's response expressed as a difference in true anomaly. Due to eccentricity of Europa's orbit, the actual westward shift of the surface patterns will oscillate around the value of the phase shift during one orbital revolution. Fig. 8 also shows that the phase shift becomes negligibly small as the rheological behavior of the asthenosphere becomes nearly elastic ($\eta_{ast} \geq 10^{16}$ Pa s) or nearly fluid ($\eta_{ast} \leq 10^{13}$ Pa s). As a result, we can conclude that viscoelasticity only influences the diurnal stress field if the characteristic Maxwell time of the asthenosphere does not deviate by approximately one order of magnitude from the inverse mean motion $1/n$.

The diurnal stress field resulting from our modeling closely resembles the results published in previous studies (Greenberg et al., 1998; Harada and Kurita, 2006; Wahr et al., 2009). However, some differences arise from the Maxwell viscoelastic treatment of the interior's rheology, the non-zero obliquity, incompressibility and the use of different interior models. As partially shown in Fig. 7, the viscoelastic representation of the tidal response leads to variations up to 20% in the magnitude of diurnal stresses. As mentioned above, viscoelasticity might also shift the entire stress field in westward direction, especially if the relaxation time of the strong transient mode T_2 is comparable to the inverse of Europa's mean motion. These typical viscoelastic effects are not observed in the surface stress modeling by Greenberg et al. (1998) and Harada and Kurita (2006), as they assume a perfectly elastic tidal response; neither in the modeling by Wahr et al. (2009), as they only explicitly show cases for which viscoelasticity becomes unimportant. In addition, our modeling of the obliquity's effect on surface diurnal stresses resembles the modeling by Rhoden et al. (2010) for nearly elastic bodies. Obviously, some differences arise from our viscoelastic treatment.

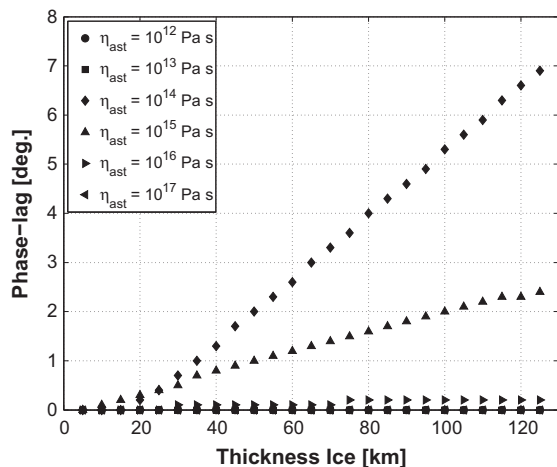


Fig. 8. Phase shift of diurnal stress field as a function of the thickness of the entire ice layer and the viscosity of the asthenosphere. In all cases, the bottom of the ocean is set at 130 km from the surface, the rigidity of ice at $\mu_{ice} = 3.487$ GPa, the eccentricity at $e = 0.0094$ and the obliquity at $\varepsilon = 0^\circ$.

In contrast to diurnal stresses, NSR stresses at the surface of Europa might experience severe relaxation effects depending on the rheological properties of the lithosphere. The relaxation state of NSR stresses at Europa's surface depends on the dimensionless parameter Δ , which is proportional to the ratio between the period of NSR and the Maxwell relaxation time of the lithosphere (see Eq. (71)). As shown by Figs. 2 and 3, viscoelastic relaxation starts to affect the magnitude and spatial distribution of NSR stresses for $\Delta > 0.1$ and becomes more severe as Δ increases. At $\Delta = 100$, viscoelastic relaxation already reduces the magnitude of NSR stresses by two orders of magnitude and shifts the entire stress field by nearly 45° in westward direction.

In the particular case of our reference model of Europa's interior, the Maxwell relaxation time of the lithosphere is equal to about 9100 years and hence $\Delta = 0.1$ would correspond to a period of NSR approximately equal to 11500 years. This value for T_{ns} is slightly smaller than the assumed minimum value for T_{ns} (12000 years), meaning that the NSR stress field at the surface of our reference model will always show signs of viscoelastic relaxation. The effects of viscoelastic relaxation are clearly visible in Fig. 9, where the NSR stress field at Europa's surface is depicted for $\Delta = 0.1, 1, 10$ and 100. There, we clearly observe that an increasing Δ leads to a gradual decrease of the magnitude of NSR stresses and a gradual shift of the entire stress field in westward direction. For $\Delta = 100$, in accordance with our theoretical expectations, the magnitude of NSR stresses becomes nearly two orders of magnitude smaller than for $\Delta = 0.1$ and the entire stress field is shifted by approximately 45° in westward direction. The exact value of the longitudinal shift does not depend on the viscoelastic response of Europa's interior, as shown by Figs. 10 and 11; at least for our reference model of Europa's interior.

However, the situation is different for other models of Europa's interior, especially if the viscosity of the asthenosphere is increased towards 10^{16} Pa s or more. In the high-viscous range, i.e. $\eta_{ast} \geq 10^{16}$ Pa s, the magnitude of the largest NSR stresses will strongly depend on the thickness and viscosity of the asthenosphere (Figs. 10 and 11). The strong dependence on the properties of the asthenosphere is caused by the relaxation of the ocean–ice boundary, represented by the buoyancy mode M_2 . In the high-viscous range (i.e. $\eta_{ast} \geq 10^{16}$ Pa s), this relaxation mode is characterized by having the slowest relaxation time of all induced modes and by having a notoriously large tangential modal strength I_{2j}^v . As a result, the effect of M_2 on NSR stresses is negligibly small for values of Δ corresponding to elastic storage of stresses or even moderate relaxation (i.e. $\Delta < 1$). The effect of M_2 on NSR stresses clearly increases as relaxation becomes more severe, leading to the large deviations observed in Fig. 11 for $\Delta = 100$. In our modeling, the relaxation mode M_2 can become sufficiently strong for $\eta_{ast} \geq 10^{17}$ Pa s and $\Delta \geq 100$ to shift the entire NSR stress field by more than 45° in westward direction, altering the usual orientation of the NSR stress patterns.

Although viscoelastic relaxation severely reduces the magnitude of NSR stresses, the NSR stress field remains larger than the ever-acting diurnal stress field for $\Delta < 43^\circ$ (i.e. $T_{ns} < 4.9$ Myr in the case of our reference model). That means that NSR stresses will dominate the state of stresses at Europa's surface if the lithosphere is sufficiently 'elastic' to prevent strong viscoelastic relaxation or if NSR is sufficiently fast to reduce the value of the ratio Δ . In other cases, the state of stresses at Europa's surface will be dominated by the diurnal stress field.

7. Conclusions and discussion

The main goal for modeling tidal stresses at Europa's surface is to study the origin and formation of the observed tectonic features.

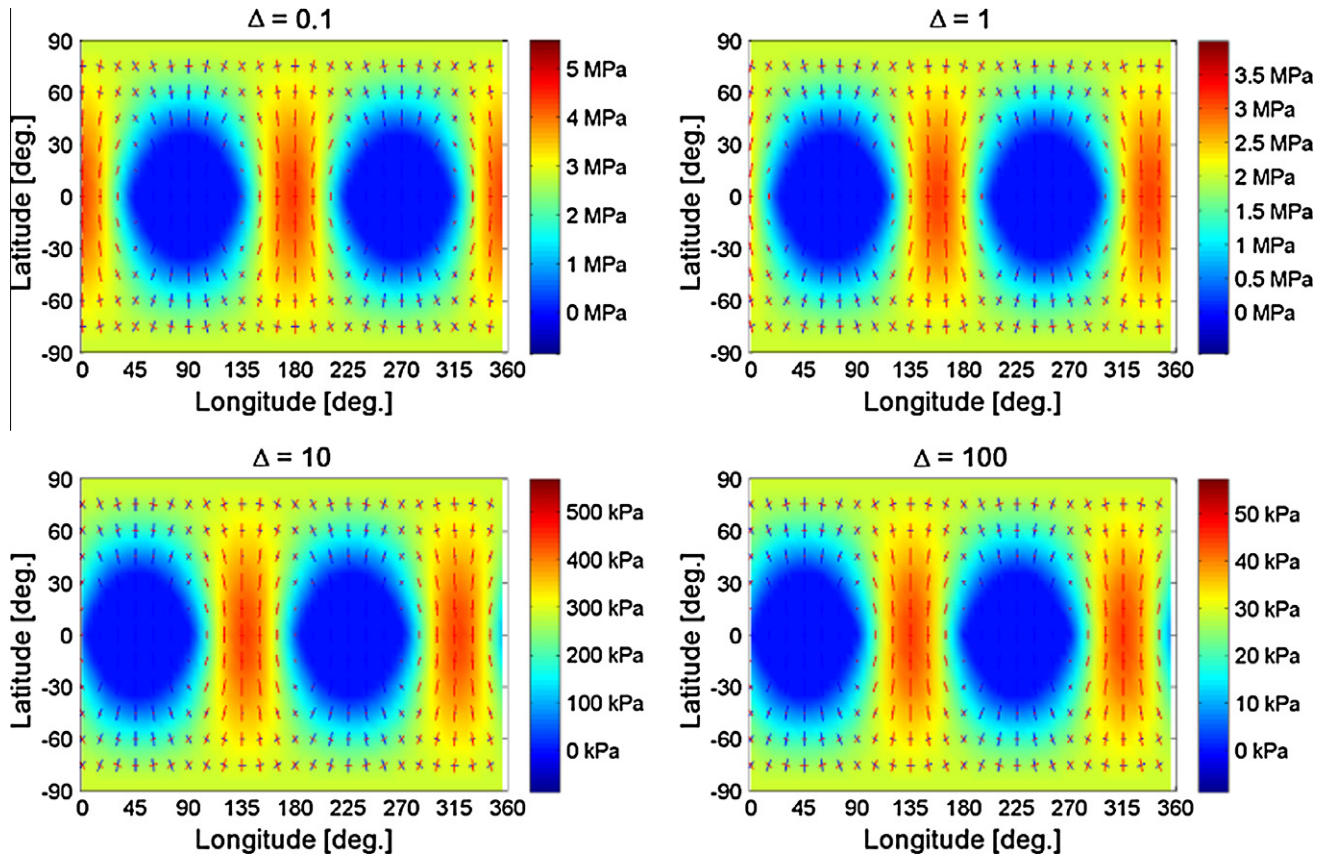


Fig. 9. NSR stress field at the surface of the reference model of Europa's interior as a function of the ratio $\Delta = \frac{\mu\eta}{20m}$. For the rheological properties of the reference model of Europa's interior, $\Delta = 0.1$ corresponds to $T_{ns} = 11419$ years, $\Delta = 1$ to $T_{ns} = 114188$ years, $\Delta = 10$ to $T_{ns} \approx 1.14$ Myr and $\Delta = 100$ to $T_{ns} \approx 11.4$ Myr.

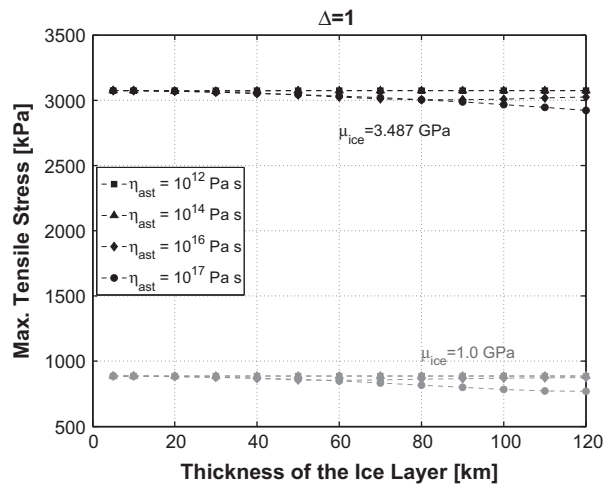


Fig. 10. Magnitude of largest NSR tensile stresses at Europa's surface as a function of the ice thickness, ice rigidity and viscosity of the asthenosphere for $\Delta = 1$. The black lines correspond to a rigidity of $\mu_{ice} = 3.487$ GPa and the gray lines to a rigidity of $\mu_{ice} = 1$ GPa.

These features are thought to have formed as a result of tensile failure of Europa's icy surface (Greenberg et al., 1998). Tensile failure most probably initiates when the acting tensile stresses exceed the tensile strength of the surface ice. Estimates of the poorly known tensile strength of ice-I at conditions relevant to Europa range from 40 kPa to several MPa, depending on porosity and contamination of the surface ice (Hoppa et al., 1999b; Schulson, 2001; Lee et al., 2005). In this paper, we have dealt with the modeling of diurnal

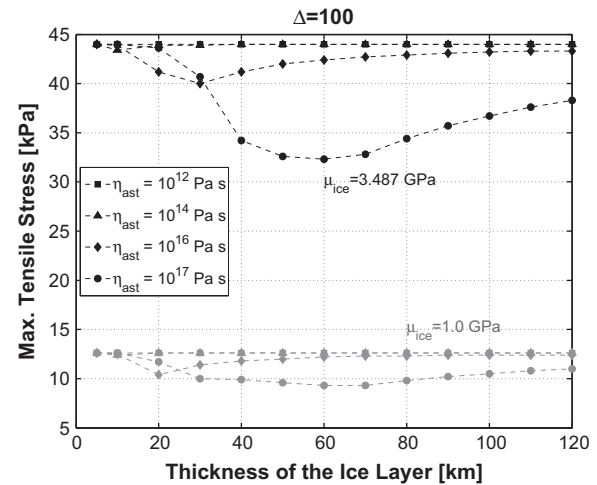


Fig. 11. Magnitude of largest NSR tensile stresses at Europa's surface as a function of the ice thickness, ice rigidity and viscosity of the asthenosphere for $\Delta = 100$. The black lines correspond to a rigidity of $\mu_{ice} = 3.487$ GPa and the gray lines to a rigidity of $\mu_{ice} = 1$ GPa.

and NSR stresses acting at Europa's surface. Diurnal stresses are often related to the origin and formation of multi-arc cycloidal features on Europa's surface, whereas NSR stresses are often required to explain the formation of long arcuate lineaments (e.g. Wahr et al., 2009).

As shown by Fig. 6, diurnal stresses at the surface of oceanless models of Europa's interior are usually much smaller than the plausible values for the tensile strength of ice. Failure of the icy

surface due to solely diurnal stresses, as suggested by the existence of numerous cycloidal lineaments on Europa's surface, would therefore require the existence of a subsurface ocean. However, diurnal stresses might exceed the tensile strength of ice if the silicate mantle would be in direct contact with an extremely low-viscous asthenosphere (η_{ast} less than $\sim 10^{12}$ Pa s). The resulting surface stress field, although large in magnitude (>100 kPa, see Fig. 6), will considerably differ from the stress field at the surface of interior models with a subsurface ocean. The question remains whether the orientation of existing cycloids can be explained by the diurnal stress field at the surface of an oceanless Europa.

The presence of a subsurface ocean, however, does not inherently guarantee that the acting diurnal stresses can be large enough to cause failure of the icy surface. As shown in Fig. 7, diurnal stresses do not exceed the tensile strength of ice when the rigidity of the icy lithosphere is assumed to be as low as 1 GPa. However, due to our poor knowledge regarding the mechanical strength of Europa's surface ice, we cannot preclude the possibility that diurnal cracking would occur for such a low rigidity. On the other hand, the sole effect of diurnal stresses could lead to mechanical failure of a 10 GPa icy lithosphere, but only if the tensile strength of the surface ice remains lower than ≈ 300 kPa. This result strongly suggests that diurnal formation of cycloidal features would preclude the existence of a non-contaminated, non-porous upper lithosphere. In addition, as shown by Fig. 5, a non-zero obliquity breaks the north-south symmetry of the diurnal stress field, allowing for an explanation for equator-crossing cycloidal features (Hurford et al., 2009).

If one takes into account that Europa's ice shell would rotate faster than synchronous, tensile stresses up to several MPa might be induced at the surface, depending on the rheological properties of the lithosphere and the rate of non-synchronous rotation. Since NSR is assumed to be a slow process ($>10^4$ years), the magnitude of NSR stresses at Europa's surface can be severely reduced by viscoelastic relaxation (see Section 6). The amount of viscoelastic relaxation acting on NSR stresses is physically described by the parameter Δ , which is directly proportional to the ratio between the period of NSR and the Maxwell time of the lithosphere. As a result, slow NSR and low-values for the viscosity of the icy lithosphere would lead to an increase of the ratio Δ , enhancing viscoelastic relaxation of NSR stresses.

NSR stresses, if present, do not act alone on Europa's surface but superimpose upon the ever-acting diurnal stresses. Variations in the value of Δ , i.e. in the relaxation state of NSR stresses, can reduce or enhance the importance of NSR stresses relative to diurnal stresses and lead to changes in the spatial and temporal distribution of the combined stress field. Without the effect of viscoelastic relaxation (i.e. $\Delta < 0.1$), NSR stresses would be much larger than diurnal stresses (approximately a factor 42 in the case of our standard model as shown by Figs. 4 and 9 for $\Delta = 0.1$). Hence, the spatial and temporal distribution of the NSR-diurnal stress patterns will hardly change on a diurnal scale. Increasing the effect of viscoelastic relaxation on NSR stresses towards $\Delta \approx 30$ gradually enhances the effect of diurnal stresses on the combined field. The combined NSR-diurnal stress field experiences periodic longitudinal oscillations on a diurnal timescale, which gradually become larger as Δ increases. When Δ becomes larger than ~ 30 (depending on the interior's model), longitudinal oscillations of the combined stress field can no longer be sustained by the strongly relaxed NSR stress field. The combined stress field would then become diurnal-like, as can be observed from Fig. 12.

We can use the combined NSR-diurnal stress field to analyze the formation of the diverse lineament morphologies observed on Europa's surface. The formation of long arcuate lineaments requires either a slowly-changing stress field or unrealistically fast crack propagation speeds. The combined NSR-diurnal stress field remains nearly static as long as the NSR component clearly domi-

nates the spatial-temporal distribution of the surface stress patterns. In our modeling, the NSR component keeps the combined stress field nearly static for values of Δ approximately smaller than 5 (equivalent to about 8° of NSR). On the other hand, the formation of cycloidal features requires a highly-variable stress field and slow crack propagation speeds. The combined NSR-diurnal stress field becomes highly-variable (diurnal-like) for values of Δ larger than 30 (equivalent to about 2° of NSR). An interesting characteristic of Europa's surface is that cycloidal features coexist with global arcuate lineaments, implying variations of the relaxation parameter Δ throughout the geological history of Europa's surface. Temporal variations of the relaxation parameter Δ can either be caused by secular variations in the rotation rate of Europa's ice shell, changes in the rheological properties of the surface ice, or both of them. Changes in tidal heat dissipation with time, due to, e.g. the time evolution of the orbit's eccentricity (Hussmann and Spohn, 2004), could then lead to changes in the ice shell thickness distribution with time, affecting Europa's rotation rate (through the principal moments of inertia of the shell) and thereby the relaxation parameter Δ . Moreover, the same changes in tidal dissipation could also induce variations in the viscosity of the icy surface and Δ (Wahr et al., 2009). Consequently, variations of the relaxation parameter Δ as a function of time strongly suggests the existence of a dynamic ice layer covering a subsurface ocean.

It is worth to mention that the methodology presented in Sections 4 and 5 implicitly assumes that Europa's interior behaves as an incompressible Maxwell body. However, the effects of compressibility are known to be generally small (less than about 20% in magnitude (Sabadini and Vermeersen, 2004)). At the same time, we consider the assumption of linear rheology of more severe influence as the rheology of planetary ices is known to be best described by non-Newtonian rheological models (Durham et al., 1997, 2001; Goldsby and Kohlstedt, 2001). The study of Europa's surface stress field from a non-Newtonian perspective is inherently numerical and depends strongly on the poorly known properties of ice-I at European conditions. Nevertheless, the dependence of the effective viscosity on the stress (non-linear effect) is small compared to the dependence on the temperature (Showman and Han, 2004), as diffusion creep might be the dominating flow mechanism for all grain sizes (Moore, 2006). By comparing our results with simulations from the viscoelastic SatStress software of Wahr et al. (2009), we obtain differences in magnitude up to $\sim 20\%$ for equivalent interior models; i.e. much less than the differences caused by the poorly constrained rigidity of ice (see Fig. 7). We assign the obtained differences in magnitude to compressibility and partially to the fact that we treated Europa's inner structure as differentiated into a liquid metallic core and a rocky mantle, whereas Wahr et al. (2009) considered a single homogeneous core/mantle layer with a higher density than our silicate mantle. Although the effect of compressibility on the magnitude of surface tidal stresses is similar to, e.g. the influence of a low-viscous asthenosphere, it is less important for our purposes as compressibility does not affect the orientation of the global stress patterns.

The purpose of this paper has been to determine the influence of a viscoelastic interior and a non-zero obliquity on diurnal and NSR stresses. We have shown that diurnal stresses at Europa's surface might experience the effects of viscoelastic relaxation of the asthenosphere, mainly in the form of a longitudinal shift of the surface stress patterns. However, as discussed in Section 6, the relevance of the viscoelastic effect is limited to interior models with a thick and highly dissipative asthenosphere. On timescales relevant for NSR ($>10^4$ years) the magnitude and phase shift of NSR surface stresses can be affected by viscoelastic relaxation of the ocean-ice boundary. This effect, however, becomes only important when NSR stresses experience strong viscoelastic relaxation in the lithospheric shell (i.e. $\Delta \sim 100$ or larger). The combination of NSR

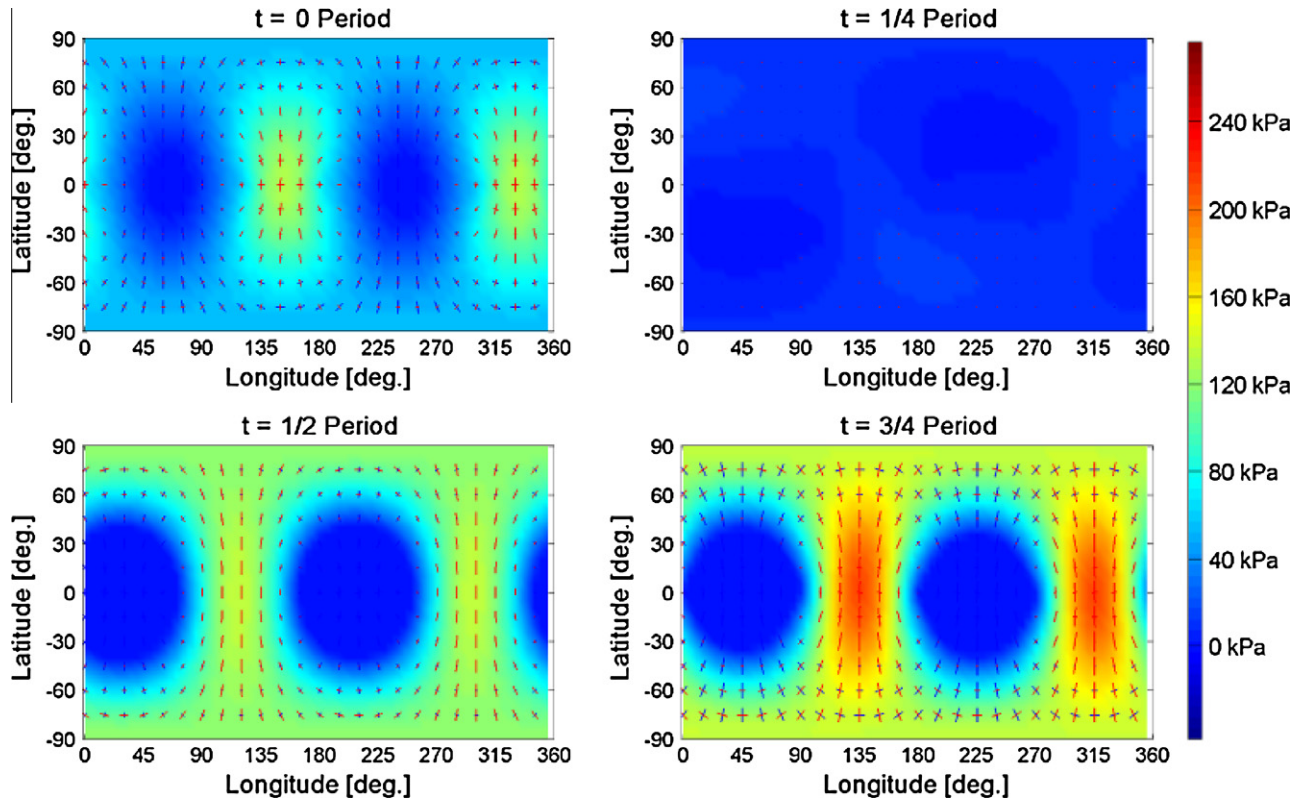


Fig. 12. Combined diurnal-NSR stress field at the surface of our reference model of Europa for $\Delta = 40^\circ$, $e = 0.0094$ and $\varepsilon = 0.1^\circ$. The stress patterns are given at four different positions on Europa's orbit around Jupiter.

and diurnal stresses for different amounts of viscoelastic relaxation of NSR stresses in the lithosphere leads to a large variety of global stress fields that might explain the formation of the large diversity of lineament morphologies observed on Europa's surface.

In addition, we have shown that even a small obliquity breaks the symmetric distribution of surface stress patterns with respect to the equator. The effect of a small obliquity on the local magnitude and orientation of diurnal stress patterns is largest at mid-latitudes and when Europa is located 90° away from the nodes formed by the intersection of Europa's orbital and equatorial planes (see Fig. 5). In those cases, local differences in magnitude up to more than 100% with respect to the eccentricity-only case are possible, even for very small obliquities ($<0.25^\circ$). Diurnal stresses induced by the obliquity can offer an explanation for the existence of equator-crossing cycloids and the southern shift of the Wedges region, as suggested by Hurford et al. (2009) and Rhoden et al. (2010).

Acknowledgments

The authors would like to thank Bruce Bills and an anonymous reviewer for their constructive comments and suggestions on the manuscript, Zane A. Selvens for sharing the SatStress model with the scientific community, and Luuk van Barneveld, Marco Kleuskens and Elja Huibregtse for contributions to the theoretical development of the propagator matrix technique for viscoelastic planetary bodies with internal oceans. This research has been financially supported by the GO program of the Netherlands Organization for Scientific Research (NWO).

Appendix A. Propagator matrix technique for planetary bodies with internal oceans

In Section 4 we shortly introduced a methodology to adapt the propagator matrix technique to compute the tidal response of

planetary bodies with an internal liquid ocean. In this Appendix, we will present the required adaptations to the method of Sabadini and Vermeersen (2004) in some mathematical detail. In Appendices A.1 and A.2 we present the propagator matrices applicable to, respectively, viscoelastic and fluid layers. Thereafter, in Section A.3, we discuss the boundary conditions at the mantle–ocean interface and at the ocean–ice interface. These boundary conditions are then used to couple the tidal response of the ice shell to the response of the silicate mantle underneath the putative ocean. Development of this last step (Appendix A.4) leads to a different propagator matrix, which can be used to calculate the tidal response at the surface of planetary bodies with internal oceans.

In our modeling, the layered internal structure of an icy moon with N layers is presented in the following way: layers $1 \leq i \leq n-1$ represent the ice shell, layer $i = n$ represents the liquid ocean, layers $n+1 \leq i \leq N-1$ represent the silicate mantle and layer $i = N$ is the fluid core (see Fig. A.1).

A.1. Viscoelastic propagator matrix

The propagation of the response through a viscoelastic layer is defined by the set of differential Eqs. (19)–(24). This set of differential equations can alternatively be written as (Sabadini and Vermeersen, 2004)

$$\tilde{\mathbf{y}}_l(r, s) = \tilde{\mathbf{Y}}_l(r, s) \tilde{\mathbf{C}}_l, \quad (\text{A.1})$$

where $\tilde{\mathbf{y}}_l(r, s)$ is the solution vector containing the six radial functions, $\tilde{\mathbf{Y}}_l(r, s)$ is the 6×6 fundamental matrix given by Eq. (1.74) of Sabadini and Vermeersen (2004) and $\tilde{\mathbf{C}}_l$ is a 6×1 vector of integration constants.

An important property of the radial functions \tilde{y}_1 to \tilde{y}_6 is that they are continuous at every internal boundary between two viscoelastic layers. Hence, the following condition holds at the boundary $r = r_{i+1}$ between viscoelastic layers i and $i+1$:

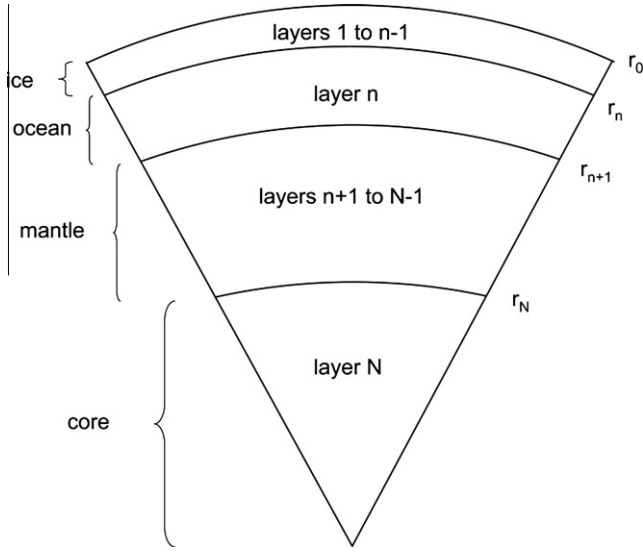


Fig. A.1. Definition of the nomenclature used to describe the internal layers of Europa. Layers $1 \leq i \leq n-1$ are the ice shell, layer $i=n$ is the ocean, layers $n+1 \leq i \leq N-1$ are the solid mantle and layer $i=N$ is the fluid core.

$$\tilde{\mathbf{Y}}_l^{(i)}(r_{i+1}, s) \tilde{\mathbf{C}}_l^{(i)} = \tilde{\mathbf{Y}}_l^{(i+1)}(r_{i+1}, s) \tilde{\mathbf{C}}_l^{(i+1)}. \quad (\text{A.2})$$

The continuity condition of the radial functions allows us to propagate the solution vector from the base of a group of viscoelastic layers to the top of the same group of layers. In the particular case of planetary satellites with a subsurface ocean we can propagate the complete viscoelastic solution within two regions, namely:

- *The mantle:* the solution vector at the top of the mantle $\tilde{\mathbf{y}}_l^{(n+1)}(r_{n+1}, s)$ can be related to the conditions at the core mantle boundary (CMB) by

$$\tilde{\mathbf{y}}_l^{(n+1)}(r_{n+1}, s) = \left(\prod_{i=n+1}^{N-1} \tilde{\mathbf{Y}}_l^{(i)}(r_i, s) \left(\tilde{\mathbf{Y}}_l^{(i)}(r_{i+1}, s) \right)^{-1} \right) \tilde{\mathbf{y}}_l^{(N)}(r_N), \quad (\text{A.3})$$

where the inverse of the fundamental matrix $\tilde{\mathbf{Y}}_l(r, s)$ is defined by Eqs. (1.75)–(1.77) of Sabadini and Vermeersen (2004). Moreover, since we assume that the core is an inviscid fluid, we can express the solution vector at the CMB as (Sabadini and Vermeersen, 2004)

$$\tilde{\mathbf{y}}_l^{(N)}(r_N) = \tilde{\mathbf{I}}_{c,l}(r_N) \tilde{\mathbf{C}}_{c,l}, \quad (\text{A.4})$$

where $\tilde{\mathbf{I}}_{c,l}(r_N)$ is the 6×3 interface matrix defined by Eq. (1.103) of Sabadini and Vermeersen (2004) and $\tilde{\mathbf{C}}_{c,l} = (K_1, K_2, K_3)^T$ is a 3-component constant vector.

As a matter of convenience we define

$$\tilde{\mathbf{B}}_l^{sm} = \prod_{i=n+1}^{N-1} \tilde{\mathbf{Y}}_l^{(i)}(r_i, s) \left(\tilde{\mathbf{Y}}_l^{(i)}(r_{i+1}, s) \right)^{-1} \tilde{\mathbf{I}}_{c,l}(r_N) \quad (\text{A.5})$$

as the mantle propagator matrix. Hence, Eq. (A.3) can be alternatively expressed as:

$$\tilde{\mathbf{y}}_l^{(n+1)}(r_{n+1}, s) = \tilde{\mathbf{B}}_l^{sm} \tilde{\mathbf{C}}_{c,l}. \quad (\text{A.6})$$

- *The ice shell:* in a similar way, we can relate the solution vector at the surface to the conditions at the ocean–ice boundary by

$$\tilde{\mathbf{y}}_l^{(1)}(R, s) = \tilde{\mathbf{B}}_l^{si} \tilde{\mathbf{y}}_l^{(n)}(r_n), \quad (\text{A.7})$$

where the ice propagator matrix $\tilde{\mathbf{B}}_l^{si}$ is defined by

$$\tilde{\mathbf{B}}_l^{si} = \prod_{i=1}^{n-1} \tilde{\mathbf{Y}}_l^{(i)}(r_i, s) \left(\tilde{\mathbf{Y}}_l^{(i)}(r_{i+1}, s) \right)^{-1}. \quad (\text{A.8})$$

A.2. Fluid propagator matrix

As stated in Section 4.2, the presence of a subsurface ocean precludes the propagation of mechanical quantities (i.e. deformations and stresses) from the top of the mantle to the base of the ice shell, thereby implying that only the perturbed gravitational potential ($\tilde{y}_5 = -\tilde{\Phi}_l$) and its radial derivative ($\tilde{y}_7 = \tilde{Q}_l^*$) can be propagated through the liquid ocean. As a result, the response of the ice shell is mechanically decoupled from the response of the mantle, albeit remaining gravitationally coupled.

The propagation of the gravity-related radial functions \tilde{y}_5 and \tilde{y}_7 through a liquid layer is governed by the set of differential Eqs. (25) and (26). This set of equations can alternatively be written as

$$\begin{pmatrix} -\tilde{\Phi}_l \\ \tilde{Q}_l^* \end{pmatrix} = \begin{pmatrix} r^l & r^{-(l+1)} \\ l r^{l-1} & -(l+1) r^{-(l+2)} \end{pmatrix} \begin{pmatrix} C_1 \\ C_2 \end{pmatrix} = \tilde{\mathbf{H}}_l(r, s) \tilde{\mathbf{C}}_l, \quad (\text{A.9})$$

where $\tilde{\mathbf{H}}_l$ is the fundamental matrix and $\tilde{\mathbf{C}}_l$ is a vector of integration constants.

In contrast to all other radial functions, \tilde{Q}_l^* is characterized by being discontinuous at the interface between two fluid layers with different densities and at the boundaries with viscoelastic layers. Since we want to keep the number of discontinuous boundaries as low as possible (i.e. two boundaries), we simplify the modeling by assuming that the density is constant throughout the entire ocean layer. As a result, we can relate the solution vector at the top of the ocean to the solution vector at the bottom of the ocean by

$$\begin{pmatrix} -\tilde{\Phi}_l^{(n)}(r_n) \\ \tilde{Q}_l^{*(n)}(r_n) \end{pmatrix} = \tilde{\mathbf{B}}_l^f \begin{pmatrix} -\tilde{\Phi}_l^{(n)}(r_{n+1}) \\ \tilde{Q}_l^{*(n)}(r_{n+1}) \end{pmatrix}, \quad (\text{A.10})$$

in which $\tilde{\mathbf{B}}_l^f$ is the fluid propagator matrix defined by

$$\tilde{\mathbf{B}}_l^f = \tilde{\mathbf{H}}_l^{(n)}(r_n, s) \left(\tilde{\mathbf{H}}_l^{(n)}(r_{n+1}, s) \right)^{-1}. \quad (\text{A.11})$$

The situation would be slightly more complicated for stratified oceans, as each additional boundary would result in an additional discontinuity in \tilde{Q}_l^* .

A.3. Boundary conditions

As can be seen from Eq. (A.10) only two elements of the solution vector are propagated through fluid layers, whereas propagation through viscoelastic layers requires all six elements of the solution vector. A proper set of boundary conditions is required to express the conditions at the viscoelastic side of a fluid–solid interface in terms of the conditions at the fluid side of the same interface. In the case of a subsurface ocean, we need to define such boundary conditions at two interfaces:

1. *At the ocean–ice interface:* the radial deformation of the ocean $\tilde{U}_l^{(n)}(r_n)$ cannot follow an equipotential surface as the icy shell prevents such a radial displacement. A constant term K_4 takes into account the difference between the shape of the ideal equipotential surface at the top of the ocean layer and the shape of the icy shell at its base. Furthermore, the pressure induced by this constant term K_4 defines the radial stress $\tilde{\sigma}_{r,l}^{(n)}(r_n)$ at the top of the ocean. The tangential deformation $\tilde{V}_l^{(n-1)}(r_n)$ at the base of the icy shell is assumed to be decoupled from the motion of the ocean and equal to a constant K_5 . The tangential stress at the interface is zero in the absence of acting tangential traction. By taking into account continuity of the six elements

across the ocean–ice interface and the boundary condition for the tangential deformation, we can define the set of boundary conditions at the ocean–ice interface as (adapted from Greff-Lefftz et al. (2000)):

$$\begin{pmatrix} \tilde{U}_l^{(n-1)}(r_n) \\ \tilde{V}_l^{(n-1)}(r_n) \\ \tilde{\sigma}_{rr,l}^{(n-1)}(r_n) \\ \tilde{\sigma}_{r\theta,l}^{(n-1)}(r_n) \\ -\tilde{\Phi}_l^{(n-1)}(r_n) \\ \tilde{Q}_l^{(n-1)}(r_n) \end{pmatrix} = \begin{pmatrix} \frac{\tilde{\Phi}_l^{(n)}(r_n)}{g(r_n)} + K_4 \\ K_5 \\ \rho_0^{(n)} g(r_n) K_4 \\ 0 \\ -\tilde{\Phi}_l^{(n)}(r_n) \\ \tilde{Q}_l^{(n)}(r_n) + 4\pi G \rho_0^{(n)} K_4 \end{pmatrix}, \quad (\text{A.12})$$

where the sixth element of the solution vector at the base of the icy shell, $\tilde{Q}_l^{(n-1)}(r_n)$, can alternatively be expressed as

$$\tilde{Q}_l^{(n-1)}(r_n) = \tilde{Q}_l^{*(n)}(r_n) - \frac{l+1}{r_n} \tilde{\Phi}_l^{(n)} + 4\pi G \rho_0^{(n)} \left(\frac{\tilde{\Phi}_l^{(n)}(r_n)}{g(r_n)} + K_4 \right). \quad (\text{A.13})$$

2. *At the mantle–ocean interface:* the set of boundary conditions at this interface slightly differs from the set corresponding to the ocean–ice interface (Eq. (A.12)). The first difference is related to the tangential deformation at the top of the mantle $\tilde{V}_l^{(n+1)}(r_{n+1})$, which does not propagate further to the base of the ocean as the tangential motion of both layers is assumed to be decoupled (free-slip boundary condition). The second difference is related to the radial deformation at the top of the mantle $\tilde{U}_l^{(n+1)}(r_{n+1})$, which at this boundary is defined as the difference between the equipotential shape and a constant K_6 (Greff-Lefftz et al., 2000). By taking these observations into account, the set of boundary conditions at the mantle–ocean interface can be written as (adapted from Greff-Lefftz et al. (2000)):

$$\begin{pmatrix} \frac{\tilde{\Phi}_l^{(n)}(r_{n+1})}{g(r_{n+1})} \\ \tilde{V}_l^{(n)}(r_{n+1}) \\ \tilde{\sigma}_{rr,l}^{(n)}(r_{n+1}) \\ \tilde{\sigma}_{r\theta,l}^{(n)}(r_{n+1}) \\ -\tilde{\Phi}_l^{(n)}(r_{n+1}) \\ \tilde{Q}_l^{(n+1)}(r_{n+1}) \end{pmatrix} = \begin{pmatrix} \tilde{U}_l^{(n+1)}(r_{n+1}) + K_6 \\ - \\ -\rho_0^{(n)} g(r_{n+1}) K_6 \\ 0 \\ -\tilde{\Phi}_l^{(n+1)}(r_{n+1}) \\ \tilde{Q}_l^{(n)}(r_{n+1}) - 4\pi G \rho_0^{(n)} K_6 \end{pmatrix}, \quad (\text{A.14})$$

where the sixth element of the solution vector at the top of the mantle, $\tilde{Q}_l^{(n+1)}(r_{n+1})$, can also be written as

$$\tilde{Q}_l^{(n+1)}(r_{n+1}) = \tilde{Q}_l^{*(n)}(r_{n+1}) - \frac{l+1}{r_{n+1}} \tilde{\Phi}_l^{(n)}(r_{n+1}) + 4\pi G \rho_0^{(n)} \left(\frac{\tilde{\Phi}_l^{(n)}(r_{n+1})}{g(r_{n+1})} - K_6 \right). \quad (\text{A.15})$$

These additional boundary conditions increase the level of complexity of the propagator matrix technique, as will be shown in Appendix A.4.

A.4. Application to icy moons I: normal modes

Following the procedure presented in Sabadini and Vermeersen (2004) we start the determination of the tidal response by computing the M relaxation modes of a predefined interior model. Theoretical studies on the number of relaxation modes corresponding to a given model of the interior have lead to the following result (see Sabadini and Vermeersen, 2004):

- The surface contributes one mode, labeled M_0 .
- At the boundary between two viscoelastic layers or one viscoelastic and one fluid layer, one buoyancy mode M_i ($i = 1, 2, 3, \dots$) is triggered if the density on both sides of the boundary is different.
- At the boundary between two viscoelastic layers, two additional modes T_i ($i = 1, 2, 3, \dots$) are triggered if the Maxwell time $\tau_M = \frac{\mu}{\eta}$ on both sides of the boundary is different. These paired modes are called transient modes as they have relatively short relaxation times.
- The core–mantle boundary (CMB) contributes one mode, labeled C_0 .

In order to determine which relaxation modes are applicable to our interior models, we need to find the M non-zero roots of the secular determinant

$$\det(\tilde{\mathbf{W}}_1) = 0. \quad (\text{A.16})$$

These roots, which we compute numerically by applying Ridders' method (e.g. Press et al., 1996) to the equation above, are defined as the inverse relaxation times s_j ($j = 1, 2, \dots, M$) of the interior model or, alternatively, as the free oscillations of the model. The roots are the solutions of the characteristic equation

$$\mathbf{0} = \tilde{\mathbf{W}}_1 \tilde{\mathbf{C}}_{\text{icy},l}, \quad (\text{A.17})$$

where $\tilde{\mathbf{C}}_{\text{icy},l} = (K_4 \ K_5 \ K_1 \ K_2 \ K_3)^T$ is the 5×1 vector of unknowns and $\tilde{\mathbf{W}}_1$ is the 5×5 propagator matrix defined by (see Appendix B for derivation)

$$\tilde{\mathbf{W}}_1 = \begin{pmatrix} 0 & 0 & L_{l,1} & L_{l,2} & L_{l,3} \\ 0 & 0 & \tilde{\mathbf{B}}_{l,41}^{sm} & \tilde{\mathbf{B}}_{l,42}^{sm} & \tilde{\mathbf{B}}_{l,43}^{sm} \\ R_{l,3} & \tilde{\mathbf{B}}_{l,32}^{si} & G_{l,11} & G_{l,12} & G_{l,13} \\ R_{l,4} & \tilde{\mathbf{B}}_{l,42}^{si} & G_{l,21} & G_{l,22} & G_{l,23} \\ R_{l,6} & \tilde{\mathbf{B}}_{l,62}^{si} & G_{l,31} & G_{l,32} & G_{l,33} \end{pmatrix}. \quad (\text{A.18})$$

Eq. (A.18) contains four groups of elements, each of them having a specific relation to the unknown constants K_1 to K_5 . The first group includes the nine terms $G_{l,yw}$ (row $1 \leq v \leq 3$ and column $1 \leq w \leq 3$), which are explicitly defined by Eq. (B.11). These terms describe the propagation of the conditions at the CMB to the surface. The second group includes the terms $R_{l,y}$ and $\tilde{\mathbf{B}}_{l,y2}^{si}$ ($y \in \{3, 4, 6\}$), which are respectively defined by Eqs. (B.7) and (A.8). These terms together describe the propagation of the conditions at the ocean–ice boundary to the surface. The third group contains the terms $\tilde{\mathbf{B}}_{l,4x}^{sm}$ ($x \in \{1, 2, 3\}$), which are defined by Eq. (A.5). This group of terms denotes the boundary condition on the tangential stress at the mantle–ocean boundary. Finally, the fourth group includes the terms $L_{l,x}$ ($x \in \{1, 2, 3\}$), which are defined by Eq. (B.16). These terms represent the boundary condition on the radial deformation at the mantle–ocean boundary. The last two conditions can be safely used as both the tangential stress and the radial deformation at the mantle–ocean boundary cannot be propagated through the ocean layer.

A.5. Application to icy moons II: impulse response to tidal forces

After determining the M normal modes of our interior model and their corresponding relaxation times and modal strengths, we proceed with the computation of the response of our interior model to a unit impulse tidal forcing. This so-called unit impulse response of the interior to the acting tides is a property of the interior and hence it does not depend on the forcing itself.

Tidal forces constrain the parameters $\tilde{\sigma}_{rr,l}$, $\tilde{\sigma}_{r\theta,l}$ and \tilde{Q}_l of the solution vector at the surface, such that the boundary condition vector $\tilde{\mathbf{b}}$ becomes (adapted from Sabadini and Vermeersen (2004))

$$\tilde{\mathbf{b}} = \begin{pmatrix} 0 & 0 & 0 & 0 & -\frac{(2l+1)}{R} \end{pmatrix}^T, \quad (\text{A.19})$$

where the last three elements refer to the boundary conditions at the surface and the first two refer to the additional boundary conditions at the mantle–ocean boundary (see Appendix B for a more detailed explanation).

The boundary condition vector $\tilde{\mathbf{b}}$ provides five constraints, which can be related to the unknown constants K_1 to K_5 by means of the propagator matrix $\tilde{\mathbf{W}}_1$ (Eq. (A.18)); i.e

$$\tilde{\mathbf{b}} = \tilde{\mathbf{W}}_1 \tilde{\mathbf{C}}_{icy,l}. \quad (\text{A.20})$$

In a similar way, we can relate the remaining three elements of the solution vector at the surface (i.e. \tilde{U}_l , \tilde{V}_l and $-\tilde{\Phi}_l$) to the conditions at the CMB and ocean–ice boundary (i.e. K_1 to K_5) by means of a different propagator matrix, which we will denote as $\tilde{\mathbf{W}}_2$. After some analytical manipulation we can express the unconstrained part of Eq. (B.1) as

$$\tilde{\mathbf{X}}_l(s) = \begin{pmatrix} \tilde{U}_l(R, s) \\ \tilde{V}_l(R, s) \\ -\tilde{\Phi}_l(R, s) \end{pmatrix} = \mathbf{P}_{35} \tilde{\mathbf{W}}_2 \tilde{\mathbf{C}}_{icy,l}, \quad (\text{A.21})$$

where $\tilde{\mathbf{X}}_l(s)$ is the impulse response at the surface, $\tilde{\mathbf{W}}_2$ is the propagator matrix defined by Eq. (B.20) and \mathbf{P}_{35} is a projection matrix that filters out the first two elements of the product between $\tilde{\mathbf{W}}_2$ and $\tilde{\mathbf{C}}_{icy,l}$. The derivation of the propagator matrix $\tilde{\mathbf{W}}_2$, which basically follows the same steps as the derivation of $\tilde{\mathbf{W}}_1$, is shortly outlined in Appendix B.

Thereafter, we substitute Eq. (A.20) into Eq. (A.21) in order to obtain a more convenient expression for the unit impulse response $\tilde{\mathbf{X}}_l(s)$ at the surface, i.e.:

$$\tilde{\mathbf{X}}_l(s) = \begin{pmatrix} \tilde{U}_l(R, s) \\ \tilde{V}_l(R, s) \\ -\tilde{\Phi}_l(R, s) \end{pmatrix} = \mathbf{P}_{35} \tilde{\mathbf{W}}_2 (\tilde{\mathbf{W}}_1)^{-1} \tilde{\mathbf{b}}, \quad (\text{A.22})$$

where the inverse of the propagator matrix $\tilde{\mathbf{W}}_1$ can alternatively be written as the ratio between its matrix of complementary minors $\tilde{\mathbf{W}}_1^\dagger$ and its determinant, i.e.

$$(\tilde{\mathbf{W}}_1)^{-1} = \frac{\tilde{\mathbf{W}}_1^\dagger}{\det(\tilde{\mathbf{W}}_1)}. \quad (\text{A.23})$$

Eq. (A.23) clearly shows that each of the M relaxation modes produces a singularity in the unit impulse response, because the determinant of the matrix $\tilde{\mathbf{W}}_1$ becomes zero for all $s = s_j$. As a final step, we apply complex contour integration to Eq. (A.22) to obtain the following expression for the unit impulse response to tidal forces (Sabadini and Vermeersen, 2004):

$$\tilde{\mathbf{X}}_l(s) = \begin{pmatrix} \tilde{U}_l(R, s) \\ \tilde{V}_l(R, s) \\ -\tilde{\Phi}_l(R, s) \end{pmatrix} = \mathbf{K}_l^e(R) + \sum_{j=1}^M \frac{\mathbf{K}_l^j(R)}{s - s_j}, \quad (\text{A.24})$$

in which the elastic limit parameter $\mathbf{K}_l^e(R)$ is given by

$$\mathbf{K}_l^e(R) = \lim_{s \rightarrow \infty} \mathbf{P}_{35} \tilde{\mathbf{W}}_2 (\tilde{\mathbf{W}}_1)^{-1} \tilde{\mathbf{b}}, \quad (\text{A.25})$$

and the vector residues $\mathbf{K}_l^j(R)$ are given by

$$\mathbf{K}_l^j(R) = \mathbf{P}_{35} \left(\frac{\tilde{\mathbf{W}}_2 (\tilde{\mathbf{W}}_1^\dagger)}{\frac{d}{ds} \det(\tilde{\mathbf{W}}_1)} \right)_{s=s_j} \tilde{\mathbf{b}}, \quad (\text{A.26})$$

where the derivative to s of the function $\det(\tilde{\mathbf{W}}_1)$ at $s = s_j$ is calculated by Ridder's method of polynomial extrapolation (Press et al., 1996).

Although Eqs. (A.24)–(A.26) already give a representation of the viscoelastic response of a planetary body to tidal forces, it is common to express the unit response in terms of the Love numbers h_2 , l_2 and k_2 . The relation between the Love numbers and the response has been discussed in Section 4.3.

Appendix B. Derivation of the propagator matrices $\tilde{\mathbf{W}}_1$ and $\tilde{\mathbf{W}}_2$

As has been discussed in Appendices A.1–A.3, the presence of an internal liquid ocean divides the propagation process into three regions of application, namely: the silicate mantle, the liquid ocean and the ice shell. Here, we combine the propagation within each of these separate regions into one single propagator matrix by explicit application of the boundary conditions given by Eqs. (A.12) and (A.14).

We start the combination process by relating the conditions at the free (unforced) surface to the solution vector at the base of the ice shell, i.e.

$$\begin{pmatrix} \tilde{U}_l^{(1)}(R) \\ \tilde{V}_l^{(1)}(R) \\ 0 \\ 0 \\ -\tilde{\Phi}_l^{(1)}(R) \\ 0 \end{pmatrix} = \tilde{\mathbf{B}}_l^{si} \begin{pmatrix} \tilde{U}_l^{(n-1)}(r_n) \\ \tilde{V}_l^{(n-1)}(r_n) \\ \tilde{\sigma}_{rr,l}^{(n-1)}(r_n) \\ \tilde{\sigma}_{r\theta,l}^{(n-1)}(r_n) \\ -\tilde{\Phi}_l^{(n-1)}(r_n) \\ \tilde{Q}_l^{(n-1)}(r_n) \end{pmatrix}, \quad (\text{B.1})$$

where $\tilde{\mathbf{B}}_l^{si}$ is the ice propagator matrix defined by Eq. (A.8).

Eq. (B.1) introduces three constraints to the propagation problem, as both stress elements ($\tilde{\sigma}_{rr,l}$ and $\tilde{\sigma}_{r\theta,l}$) and the so-called potential stress (\tilde{Q}_l) are by definition equal to zero at the surface in the free surface case (Sabadini and Vermeersen, 2004). Here, we recall that the free surface case is used to determine the normal modes or free oscillations of our interior model. The determination of these modes and their corresponding relaxation times and strengths is a very important step in the calculation of the viscoelastic response of an icy moon to tidal forces, because these modes describe the effect of viscoelastic relaxation on the response at the surface. Consequently, we proceed our discussion by only taking into account the constrained part of Eq. (A.8), i.e.

$$\mathbf{0} = \mathbf{P}_1 \tilde{\mathbf{B}}_l^{si} \begin{pmatrix} \tilde{U}_l^{(n-1)}(r_n) \\ \tilde{V}_l^{(n-1)}(r_n) \\ \tilde{\sigma}_{rr,l}^{(n-1)}(r_n) \\ \tilde{\sigma}_{r\theta,l}^{(n-1)}(r_n) \\ -\tilde{\Phi}_l^{(n-1)}(r_n) \\ \tilde{Q}_l^{(n-1)}(r_n) \end{pmatrix}, \quad (\text{B.2})$$

where the projector operator \mathbf{P}_1 is given by

$$\mathbf{P}_1 = \begin{pmatrix} 0 & 0 & 1 & 0 & 0 & 0 \\ 0 & 0 & 0 & 1 & 0 & 0 \\ 0 & 0 & 0 & 0 & 0 & 1 \end{pmatrix}. \quad (\text{B.3})$$

Thereafter, we apply the set of boundary conditions at the ocean–ice interface (Eq. (A.12)) to the right side of Eq. (B.2). This step leads to the following expression:

$$\tilde{\mathbf{d}}_s = \tilde{\mathbf{B}}_l^{R1} \begin{pmatrix} \frac{\tilde{\phi}_l^{(n)}(r_n)}{g(r_n)} \\ -\tilde{\phi}_l^{(n)}(r_n) \\ \tilde{Q}_l^{(n)}(r_n) \end{pmatrix}, \quad (\text{B.4})$$

where the matrix $\tilde{\mathbf{B}}_l^{R1}$ is defined as

$$\tilde{\mathbf{B}}_l^{R1} = \mathbf{P}_l \tilde{\mathbf{B}}_l^{si} = \begin{pmatrix} 1 & 0 & 0 \\ 0 & 0 & 0 \\ 0 & 0 & 0 \\ 0 & 0 & 0 \\ 0 & 1 & 0 \\ 0 & 0 & 1 \end{pmatrix}, \quad (\text{B.5})$$

and the vector $\tilde{\mathbf{d}}_s$ as

$$\tilde{\mathbf{d}}_s = \begin{pmatrix} -R_{l,3}K_4 - \tilde{\mathbf{B}}_{l,32}^{si}K_5 \\ -R_{l,4}K_4 - \tilde{\mathbf{B}}_{l,42}^{si}K_5 \\ -R_{l,6}K_4 - \tilde{\mathbf{B}}_{l,62}^{si}K_5 \end{pmatrix}, \quad (\text{B.6})$$

with $R_{l,y}$ ($y \in \{3, 4, 6\}$) defined by

$$R_{l,y} = \tilde{\mathbf{B}}_{l,y1}^{si} + \rho_0^{(n)} g(r_n) \tilde{\mathbf{B}}_{l,y3}^{si} + 4\pi G \rho_0^{(n)} \tilde{\mathbf{B}}_{l,y6}^{si}. \quad (\text{B.7})$$

In Eqs. (B.6) and (B.7) the subscripts refer to an individual element of the ice propagator matrix $\tilde{\mathbf{B}}_l^{si}$. By convention, the first digit in the subscript indicates the row and the second digit the column.

The next step is to express the right hand side of Eq. (B.4) in terms of the conditions at the bottom of the ocean layer. Substitution of Eqs. (A.12) and (A.13) into Eq. (B.4) yields

$$\tilde{\mathbf{d}}_s = \tilde{\mathbf{B}}_l^{R1} \begin{pmatrix} \frac{1}{g(r_n)} \left(\tilde{\mathbf{B}}_{l,11}^f \tilde{\phi}_l^{(n)}(r_{n+1}) - \tilde{\mathbf{B}}_{l,12}^f \tilde{Q}_l^{*(n)}(r_{n+1}) \right) \\ -\tilde{\mathbf{B}}_{l,11}^f \tilde{\phi}_l^{(n)}(r_{n+1}) + \tilde{\mathbf{B}}_{l,12}^f \tilde{Q}_l^{*(n)}(r_{n+1}) \\ -\tilde{\mathbf{B}}_{l,21}^f \tilde{\phi}_l^{(n)}(r_{n+1}) + \tilde{\mathbf{B}}_{l,22}^f \tilde{Q}_l^{*(n)}(r_{n+1}) + J \end{pmatrix}, \quad (\text{B.8})$$

where the auxiliary variable J is defined by

$$J = \left(\frac{l+1}{r_n} - \frac{4\pi G \rho_0^{(n)}}{g(r_n)} \right) \left(-\tilde{\mathbf{B}}_{l,11}^f \tilde{\phi}_l^{(n)}(r_{n+1}) + \tilde{\mathbf{B}}_{l,12}^f \tilde{Q}_l^{*(n)}(r_{n+1}) \right). \quad (\text{B.9})$$

Moreover, the radial functions $-\tilde{\phi}_l^{(n)}(r_{n+1})$ and $\tilde{Q}_l^{*(n)}(r_{n+1})$ at the bottom of the ocean can be expressed in terms of the conditions at the CMB by applying the set of boundary conditions at the mantle–ocean interface (Eq. (A.14)) and the viscoelastic propagation through the silicate mantle (Eq. (A.6)). Then, we can write Eq. (B.8) as follows:

$$\tilde{\mathbf{d}}_s = \begin{pmatrix} G_{l,11} & G_{l,12} & G_{l,13} \\ G_{l,21} & G_{l,22} & G_{l,23} \\ G_{l,31} & G_{l,32} & G_{l,33} \end{pmatrix} \tilde{\mathbf{C}}_{c,l}, \quad (\text{B.10})$$

where the elements $G_{l,vw}$ (row $1 \leq v \leq 3$ and column $1 \leq w \leq 3$) are defined by

$$\begin{aligned} G_{l,vw} = & -\frac{\tilde{\mathbf{B}}_{l,v1}^{R1}}{g(r_n)} \left(\tilde{\mathbf{B}}_{l,11}^f \tilde{\mathbf{B}}_{l,5w}^{sm} + \tilde{\mathbf{B}}_{l,12}^f Z_{l,w} \right) \\ & + \tilde{\mathbf{B}}_{l,v2}^{R1} \left(\tilde{\mathbf{B}}_{l,11}^f \tilde{\mathbf{B}}_{l,5w}^{sm} + \tilde{\mathbf{B}}_{l,12}^f Z_{l,w} \right) \\ & + \tilde{\mathbf{B}}_{l,v3}^{R1} \left(\tilde{\mathbf{B}}_{l,21}^f \tilde{\mathbf{B}}_{l,5w}^{sm} + \tilde{\mathbf{B}}_{l,22}^f Z_{l,w} \right) \\ & + \tilde{\mathbf{B}}_{l,v3}^{R1} \left(\frac{l+1}{r_n} - \frac{4\pi G \rho_0^{(n)}}{g(r_n)} \right) \left(\tilde{\mathbf{B}}_{l,11}^f \tilde{\mathbf{B}}_{l,5w}^{sm} + \tilde{\mathbf{B}}_{l,12}^f Z_{l,w} \right), \end{aligned} \quad (\text{B.11})$$

in which

$$Z_{l,w} = \tilde{\mathbf{B}}_{l,6w}^{sm} + \left(\frac{4\pi G \rho_0^{(n)}}{g(r_{n+1})} - \frac{l+1}{r_{n+1}} \right) \tilde{\mathbf{B}}_{l,5w}^{sm} - \frac{4\pi G}{g(r_{n+1})} \tilde{\mathbf{B}}_{l,3w}^{sm}, \quad (\text{B.12})$$

where $\tilde{\mathbf{B}}_l^{sm}$ is the mantle propagator matrix defined by Eq. (A.5).

As can be seen from Eq. (B.10), we only applied three constraints to a problem having six unknowns (K_1 to K_6). The additional constraints can be obtained from the radial functions that cannot be propagated through the ocean layer, but that are related to the CMB-constants K_1 to K_3 through the set of boundary conditions at the mantle–ocean interface. The first additional constraint is defined by taking into account continuity of radial stress at the mantle–ocean boundary. Then, based on Eqs. (A.14) and (A.6), we can write the constant K_6 in terms of the CMB-constants,

$$K_6 = -\frac{1}{\rho_0^{(n)} g(r_{n+1})} \left(\tilde{\mathbf{B}}_{l,31}^{sm} \tilde{\mathbf{B}}_{l,32}^{sm} \tilde{\mathbf{B}}_{l,33}^{sm} \right) \tilde{\mathbf{C}}_{c,l}, \quad (\text{B.13})$$

thereby reducing the number of unknowns to five (K_1 to K_5).

A second additional constraint can be introduced by taking into account continuity of tangential stress at the mantle–ocean boundary. Combination of Eqs. (A.14) and (A.6) allows us to write the following expression:

$$0 = \left(\tilde{\mathbf{B}}_{l,41}^{sm} \tilde{\mathbf{B}}_{l,42}^{sm} \tilde{\mathbf{B}}_{l,43}^{sm} \right) \tilde{\mathbf{C}}_{c,l}. \quad (\text{B.14})$$

The third and last additional constraint can be obtained from the boundary condition regarding the radial displacement at the mantle–ocean interface. By making use of Eqs. (A.6), (A.14) and (B.13) we can write the following relation:

$$0 = (L_{l,1} \ L_{l,2} \ L_{l,3}) \tilde{\mathbf{C}}_{c,l}, \quad (\text{B.15})$$

where the elements $L_{l,w}$ are defined by

$$L_{l,w} = \tilde{\mathbf{B}}_{l,1w}^{sm} - \frac{1}{\rho_0^{(n)} g(r_{n+1})} \tilde{\mathbf{B}}_{l,3w}^{sm} + \frac{1}{g(r_{n+1})} \tilde{\mathbf{B}}_{l,5w}^{sm}, \quad (\text{B.16})$$

Finally, combination of Eqs. (B.10), (B.14) and (B.15) allows us to write out the propagator matrix $\tilde{\mathbf{W}}_1$ that relates the five defined constraints to the five unknowns, i.e.

$$\tilde{\mathbf{W}}_1 = \begin{pmatrix} 0 & 0 & L_{l,1} & L_{l,2} & L_{l,3} \\ 0 & 0 & \tilde{\mathbf{B}}_{l,41}^{sm} & \tilde{\mathbf{B}}_{l,42}^{sm} & \tilde{\mathbf{B}}_{l,43}^{sm} \\ R_{l,3} & \tilde{\mathbf{B}}_{l,32}^{si} & G_{l,11} & G_{l,12} & G_{l,13} \\ R_{l,4} & \tilde{\mathbf{B}}_{l,42}^{si} & G_{l,21} & G_{l,22} & G_{l,23} \\ R_{l,6} & \tilde{\mathbf{B}}_{l,62}^{si} & G_{l,31} & G_{l,32} & G_{l,33} \end{pmatrix}, \quad (\text{B.17})$$

which satisfies the characteristic equation

$$\mathbf{0} = \tilde{\mathbf{W}}_1 \tilde{\mathbf{C}}_{icy,l}, \quad (\text{B.18})$$

where $\tilde{\mathbf{C}}_{icy,l} = (K_4 \ K_5 \ K_1 \ K_2 \ K_3)^T$.

In a similar way as for the constrained part of Eq. (B.1), we can express the unconstrained parameters at the surface directly in terms of the unknown constants K_1 to K_5 . After some analytical manipulation we obtain:

$$\tilde{\mathbf{X}}_l(s) = \begin{pmatrix} \tilde{U}_l(R, s) \\ \tilde{V}_l(R, s) \\ -\tilde{\phi}_l(R, s) \end{pmatrix} = \mathbf{P}_{35} \tilde{\mathbf{W}}_2 \tilde{\mathbf{C}}_{icy,l}, \quad (\text{B.19})$$

where $\tilde{\mathbf{X}}_l(s)$ is defined as the unit impulse response, $\tilde{\mathbf{W}}_2$ is the propagator matrix, $\tilde{\mathbf{C}}_{icy,l}$ is the vector of unknown constants and \mathbf{P}_{35} is a projection matrix that filters out the first two elements of the product between $\tilde{\mathbf{W}}_2$ and $\tilde{\mathbf{C}}_{icy,l}$. The propagator matrix $\tilde{\mathbf{W}}_2$ itself is defined by

$$\widetilde{\mathbf{W}}_2 = \begin{pmatrix} 0 & 0 & L_{l,1} & L_{l,2} & L_{l,3} \\ 0 & 0 & \widetilde{\mathbf{B}}_{l,41}^{sm} & \widetilde{\mathbf{B}}_{l,42}^{sm} & \widetilde{\mathbf{B}}_{l,43}^{sm} \\ R_{l,1} & \widetilde{\mathbf{B}}_{l,12}^{si} & G'_{l,11} & G'_{l,12} & G'_{l,13} \\ R_{l,2} & \widetilde{\mathbf{B}}_{l,22}^{si} & G'_{l,21} & G'_{l,22} & G'_{l,23} \\ R_{l,5} & \widetilde{\mathbf{B}}_{l,52}^{si} & G'_{l,31} & G'_{l,32} & G'_{l,33} \end{pmatrix}, \quad (\text{B.20})$$

where the elements $G'_{l,vw}$ (row $1 \leq v \leq 3$ and column $1 \leq w \leq 3$) are defined by

$$\begin{aligned} G'_{l,vw} = & -\frac{\widetilde{\mathbf{B}}_{l,v1}^{R2}}{g(r_n)} \left(\widetilde{\mathbf{B}}_{l,11}^f \widetilde{\mathbf{B}}_{l,5w}^{sm} + \widetilde{\mathbf{B}}_{l,12}^f Z_{l,w} \right) \\ & + \widetilde{\mathbf{B}}_{l,v2}^{R2} \left(\widetilde{\mathbf{B}}_{l,11}^f \widetilde{\mathbf{B}}_{l,5w}^{sm} + \widetilde{\mathbf{B}}_{l,12}^f Z_{l,w} \right) \\ & + \widetilde{\mathbf{B}}_{l,v3}^{R2} \left(\widetilde{\mathbf{B}}_{l,21}^f \widetilde{\mathbf{B}}_{l,5w}^{sm} + \widetilde{\mathbf{B}}_{l,22}^f Z_{l,w} \right) \\ & + \widetilde{\mathbf{B}}_{l,v3}^{R2} \left(\frac{l+1}{r_n} - \frac{4\pi G \rho_0^{(n)}}{g(r_n)} \right) \left(\widetilde{\mathbf{B}}_{l,11}^f \widetilde{\mathbf{B}}_{l,5w}^{sm} + \widetilde{\mathbf{B}}_{l,12}^f Z_{l,w} \right), \end{aligned} \quad (\text{B.21})$$

with

$$\widetilde{\mathbf{B}}_l^{R2} = \mathbf{P}_2 \widetilde{\mathbf{B}}_l^{si}, \quad (\text{B.22})$$

$$\mathbf{P}_2 = \begin{pmatrix} 1 & 0 & 0 \\ 0 & 0 & 0 \\ 0 & 0 & 0 \\ 0 & 1 & 0 \\ 0 & 0 & 1 \end{pmatrix},$$

and \mathbf{P}_2 given by

$$\mathbf{P}_2 = \begin{pmatrix} 1 & 0 & 0 & 0 & 0 & 0 \\ 0 & 1 & 0 & 0 & 0 & 0 \\ 0 & 0 & 0 & 0 & 1 & 0 \end{pmatrix}. \quad (\text{B.23})$$

Appendix C. Auxiliary variables in stress equations

The elements of the diurnal stress tensor at the surface, which are mathematically defined by Eqs. (54)–(59), depend on the Love numbers (i.e. on the properties of the interior) and the co-latitude through the Beta-functions. These functions are listed below

$$\beta_{2,0}^{\theta\theta}(\theta) = \frac{3}{4}(3h_2^e - 10l_2^e) \cos(2\theta) + \frac{3}{4}(h_2^e - 2l_2^e), \quad (\text{C.1})$$

$$\beta_{2,0}^{\theta\phi}(\theta) = \frac{3}{4}(3h_{2j}^v - 10l_{2j}^v) \cos(2\theta) + \frac{3}{4}(h_{2j}^v - 2l_{2j}^v), \quad (\text{C.2})$$

$$\beta_{2,1}^{\theta\theta}(\theta) = \frac{3}{2}(3h_2^e - 10l_2^e) \sin(2\theta), \quad (\text{C.3})$$

$$\beta_{2,1}^{\theta\phi}(\theta) = \frac{3}{2}(3h_{2j}^v - 10l_{2j}^v) \sin(2\theta), \quad (\text{C.4})$$

$$\beta_{2,2}^{\theta\theta}(\theta) = -\frac{3}{2}(3h_2^e - 10l_2^e) \cos(2\theta) + \frac{9}{2}(h_2^e - 2l_2^e), \quad (\text{C.5})$$

$$\beta_{2,2}^{\theta\phi}(\theta) = -\frac{3}{2}(3h_{2j}^v - 10l_{2j}^v) \cos(2\theta) + \frac{9}{2}(h_{2j}^v - 2l_{2j}^v), \quad (\text{C.6})$$

$$\beta_{2,0}^{\phi\phi}(\theta) = \frac{3}{4}(3h_2^e - 8l_2^e) \cos(2\theta) + \frac{3}{4}(h_2^e - 4l_2^e), \quad (\text{C.7})$$

$$\beta_{2,0}^{\phi\phi}(\theta) = \frac{3}{4}(3h_{2j}^v - 8l_{2j}^v) \cos(2\theta) + \frac{3}{4}(h_{2j}^v - 4l_{2j}^v), \quad (\text{C.8})$$

$$\beta_{2,1}^{\phi\phi}(\theta) = \frac{3}{2}(3h_2^e - 8l_2^e) \sin(2\theta), \quad (\text{C.9})$$

$$\beta_{2,1}^{\phi\phi}(\theta) = \frac{3}{2}(3h_{2j}^v - 8l_{2j}^v) \sin(2\theta), \quad (\text{C.10})$$

$$\beta_{2,2}^{\phi\phi}(\theta) = -\frac{3}{2}(3h_2^e - 8l_2^e) \cos(2\theta) + \frac{9}{2}(h_2^e - 4l_2^e), \quad (\text{C.11})$$

$$\beta_{2,2}^{\phi\phi}(\theta) = -\frac{3}{2}(3h_{2j}^v - 8l_{2j}^v) \cos(2\theta) + \frac{9}{2}(h_{2j}^v - 4l_{2j}^v), \quad (\text{C.12})$$

$$\beta_{2,1}^{\phi\phi}(\theta) = 3l_2^e \sin(\theta), \quad (\text{C.13})$$

$$\beta_{2,1}^{\phi\phi}(\theta) = 3l_{2j}^v \sin(\theta), \quad (\text{C.14})$$

$$\beta_{2,2}^{\phi\phi}(\theta) = 3l_2^e \cos(\theta), \quad (\text{C.15})$$

$$\beta_{2,2}^{\phi\phi}(\theta) = 3l_{2j}^v \cos(\theta). \quad (\text{C.16})$$

In a similar way, the NSR stress tensor at Europa's surface (Eqs. (65)–(70)) depends on the Love numbers and co-latitude through the following alpha-functions:

$$\alpha_{2,2}^{\theta\theta}(\theta) = -\frac{3}{2}(3\hat{h}_2^e - 10\hat{l}_2^e) \cos(2\theta) + \frac{9}{2}(\hat{h}_2^e - 2\hat{l}_2^e), \quad (\text{C.17})$$

$$\alpha_{2,2}^{\theta\phi}(\theta) = -\frac{3}{2}(3\hat{h}_{2j}^v - 10\hat{l}_{2j}^v) \cos(2\theta) + \frac{9}{2}(\hat{h}_{2j}^v - 2\hat{l}_{2j}^v), \quad (\text{C.18})$$

$$\alpha_{2,2}^{\phi\phi}(\theta) = -\frac{3}{2}(3\hat{h}_2^e - 8\hat{l}_2^e) \cos(2\theta) + \frac{9}{2}(\hat{h}_2^e - 4\hat{l}_2^e), \quad (\text{C.19})$$

$$\alpha_{2,2}^{\phi\phi}(\theta) = -\frac{3}{2}(3\hat{h}_{2j}^v - 8\hat{l}_{2j}^v) \cos(2\theta) + \frac{9}{2}(\hat{h}_{2j}^v - 4\hat{l}_{2j}^v), \quad (\text{C.20})$$

$$\alpha_{2,2}^{\theta\phi}(\theta) = 3\hat{l}_2^e \cos(\theta), \quad (\text{C.21})$$

$$\alpha_{2,2}^{\theta\phi}(\theta) = 3\hat{l}_{2j}^v \cos(\theta), \quad (\text{C.22})$$

where the elastic Love numbers \hat{h}_2^e and \hat{l}_2^e , and modal strengths \hat{h}_{2j}^v and \hat{l}_{2j}^v refer to the tidal response of interior models in which the silicate mantle has been assumed to behave as a fluid with respect to NSR (see Section 5.2).

References

- Anderson, J., Schubert, G., Jacobson, R., Lau, E., Moore, W., Sjogren, W., 1998. Europa's differentiated internal structure: Inferences from four Galileo encounters. *Science* 281, 2019–2022.
- Baland, R., Van Hoolst, T., 2010. Librations of the Galilean satellites: The influence of global internal liquid layers. *Icarus* 209, 651–664.
- Bills, B., 2005. Free and forced obliquities of the Galilean satellites of Jupiter. *Icarus* 175, 233–247.
- Bills, B., Nimmo, F., Karatekin, O., Van Hoolst, T., Rambaux, N., Levrard, B., Laskar, J., 2009. Rotational dynamics of Europa. In: Pappalardo, R., McKinnon, W., Khurana, K. (Eds.), *Europa*. Arizona Press Space Science Series, pp. 119–134.
- Chinnery, M., 1975. The static deformation of an Earth with a fluid core: A physical approach. *Geophys. J. Roy. Astron. Soc.* 42, 461–475.
- Durham, W., Kirby, S., Stern, L., 1997. Creep of water ices at planetary conditions: A compilation. *J. Geophys. Res.* 102, 16–293.
- Durham, W., Stern, L., Kirby, S., 2001. Rheology of ice I at low stress and elevated confining pressure. *J. Geophys. Res.* 106, 11031–11042.
- Geissler, P. et al., 1998. Evolution of lineaments on Europa: Clues from Galileo multispectral imaging observations* 1. *Icarus* 135, 107–126.
- Gleeson, D., Crawford, Z., Barr, A., Mullen, M., Pappalardo, R., Prockter, L., Stempel, M., Wahr, J., 2005. Wavy and cycloidal lineament formation on Europa from combined diurnal and nonsynchronous stresses. *Lunar Planet. Sci. Conf.* 36, Abstract 2364.
- Goldreich, P., Mitchell, J., 2010. Elastic ice shells of synchronous moons: Implications for cracks on Europa and non-synchronous rotation of Titan. *Icarus* 209, 631–638.
- Goldreich, P., Peale, S., 1966. Spin-orbit coupling in the Solar System. *Astron. J.* 71, 425–438.
- Goldsby, D., Kohlstedt, D., 2001. Superplastic deformation of ice: Experimental observations. *J. Geophys. Res.* 106, 11017–11030.
- Greeley, R. et al., 1998. Europa: Initial Galileo geological observations* 1. *Icarus* 135, 4–24.
- Greenberg, R., Weidenschilling, S., 1984. How fast do Galilean satellites spin? *Icarus* 58, 186–196.
- Greenberg, R., Geissler, P., Hoppa, G., Tufts, B., Durda, D., Pappalardo, R., Head, J., Greeley, R., Sullivan, R., Carr, M., 1998. Tectonic processes on Europa: Tidal stresses, mechanical response, and visible features. *Icarus* 135, 64–78.
- Greenberg, R., Hoppa, G., Bart, G., Hurford, T., 2003. Tidal stress patterns on Europa's crust. *Celest. Mech. Dyn. Astron.* 87, 171–188.
- Greff-Lefftz, M., Legros, H., Dehant, V., 2000. Influence of the inner core viscosity on the rotational eigenmodes of the Earth. *Phys. Earth Planet. Inter.* 122, 187–204.
- Hand, K., Chyba, C., 2007. Empirical constraints on the salinity of the European ocean and implications for a thin ice shell. *Icarus* 189, 424–438.
- Hand, K., Chyba, C., Priscu, J., Carlson, K., Nealson, K., 2009. Astrobiology and the potential of life on Europa. In: Pappalardo, R., McKinnon, W., Khurana, K. (Eds.), *Europa*. Arizona Press Space Science Series, pp. 589–629.
- Harada, Y., Kurita, K., 2006. The dependence of surface tidal stress on the internal structure of Europa: The possibility of cracking of the icy shell. *Planet. Space Sci.* 54, 170–180.
- Harada, Y., Kurita, K., 2007. Effect of non-synchronous rotation on surface stress upon Europa: Constraints on surface rheology. *Geophys. Res. Lett.* 34, L11204.

- Hoppa, G., Greenberg, R., Geissler, P., Tufts, B., Plassmann, J., Durda, D., 1999a. Rotation of Europa: Constraints from terminator and limb positions. *Icarus* 137, 341–347.
- Hoppa, G., Tufts, B., Greenberg, R., Geissler, P., 1999b. Formation of cycloidal features on Europa. *Science* 285, 1899–1902.
- Hoppa, G., Tufts, B., Greenberg, R., Geissler, P., 1999c. Strike-slip faults on Europa: Global shear patterns driven by tidal stress. *Icarus* 141, 287–298.
- Hoppa, G., Tufts, B., Greenberg, R., Hurford, T., O'Brien, D., Geissler, P., 2001. Europa's rate of rotation derived from the tectonic sequence in the Astypalaea region. *Icarus* 153, 208–213.
- Hurford, T., Sarid, A., Greenberg, R., 2007. Cycloidal cracks on Europa: Improved modeling and non-synchronous rotation implications. *Icarus* 186, 218–233.
- Hurford, T., Sarid, A., Greenberg, R., Bills, B., 2009. The influence of obliquity on European cycloid formation. *Icarus* 202, 197–215.
- Husmann, H., Spohn, T., 2004. Thermal-orbital evolution of Io and Europa. *Icarus* 171, 391–410.
- Husmann, H., Spohn, T., Wiczerkowski, K., 2002. Thermal equilibrium states of Europa's ice shell: Implications for internal ocean thickness and surface heat flow. *Icarus* 156, 143–151.
- Kattenhorn, S., 2002. Nonsynchronous rotation evidence and fracture history in the Bright Plains region, Europa. *Icarus* 157, 490–506.
- Kattenhorn, S., Hurford, T., 2009. Tectonics of Europa. In: Pappalardo, R., McKinnon, W., Khurana, K. (Eds.), *Europa*. Arizona Press Space Science Series, pp. 199–236.
- Kaula, W., 1964. Tidal dissipation by solid friction and the resulting orbital evolution. *Rev. Geophys. Space Phys.* 2, 661–685.
- Khurana, K., Kivelson, M., Stevenson, D., Schubert, G., Russell, C., Walker, R., Polansky, C., 1998. Induced magnetic fields as evidence for subsurface oceans in Europa and Callisto. *Nature* 395, 777–780.
- Kivelson, M., Khurana, K., Russell, C., Volwerk, M., Walker, R., Zimmer, C., 2000. Galileo magnetometer measurements: A stronger case for a subsurface ocean at Europa. *Science* 289, 1340–1343.
- Lee, S., Pappalardo, R., Makris, N., 2005. Mechanics of tidally driven fractures in Europa's ice shell. *Icarus* 177, 367–379.
- Leith, A., McKinnon, W., 1996. Is there evidence for polar wander on Europa? *Icarus* 120, 387–398.
- Matsuyama, I., Nimmo, F., 2008. Tectonic patterns on reoriented and despun planetary bodies. *Icarus* 195, 459–473.
- Melosh, H., 1980. Tectonic patterns on a tidally distorted planet. *Icarus* 43, 334–337.
- Moore, W., 2006. Thermal equilibrium in Europa's ice shell. *Icarus* 180, 141–146.
- Moore, W., Schubert, G., 2000. The tidal response of Europa. *Icarus* 147, 317–319.
- Nimmo, F., 2004. Stresses generated in cooling viscoelastic ice shells: Application to Europa. *J. Geophys. Res.* 109, E12001.
- Nimmo, F., Manga, M., 2009. Geodynamics of Europa's icy shell. In: Pappalardo, R., McKinnon, W., Khurana, K. (Eds.), *Europa*. Arizona Press Space Science Series, pp. 119–134.
- Ojakangas, G., Stevenson, D., 1989a. Polar wander of an ice shell on Europa. *Icarus* 81, 242–270.
- Ojakangas, G., Stevenson, D., 1989b. Thermal state of an ice shell on Europa. *Icarus* 81, 220–241.
- Pappalardo, R. et al., 1999. Does Europa have a subsurface ocean? Evaluation of the geological evidence. *J. Geophys. Res. – Planets* 104, 24015–24055.
- Peltier, W., 1974. The impulse response of a Maxwell Earth. *Rev. Geophys.* 12, 649–669.
- Preblich, B., Greenberg, R., Riley, J., O'Brien, D., 2007. Tidally driven strike-slip displacement on Europa: Viscoelastic modeling. *Planet. Space Sci.* 55, 1225–1245.
- Press, W., Teukolsky, S., Vetterling, W., Flannery, B., 1996. *Numerical Recipes in Fortran 77: The Art of Scientific Computing*. Cambridge University Press.
- Ranalli, G., 1995. *Rheology of the Earth*, second ed. Chapman and Hall.
- Rappaport, N., Iess, L., Wahr, J., Lunine, J., Armstrong, J., Asmar, S., Tortora, P., Di Benedetto, M., Racioppa, P., 2008. Can Cassini detect a subsurface ocean in Titan from gravity measurements? *Icarus* 194, 711–720.
- Rhoden, A., Militzer, B., Huff, E., Hurford, T., Manga, M., Richards, M., 2010. Constraints on Europa's rotational dynamics from modeling of tidally-driven fractures. *Icarus* 210, 770–784.
- Rhoden, A., Hurford, T., Manga, M., 2011. Strike-slip fault patterns on Europa: Obliquity or polar wander? *Icarus* 211, 636–647.
- Roberts, J., Nimmo, F., 2008. Tidal heating and the long-term stability of a subsurface ocean on Enceladus. *Icarus* 194, 675–689.
- Sabadini, R., Vermeersen, L., 2004. *Global Dynamics of the Earth: Applications of Normal Mode Relaxation Theory to Solid-Earth Geophysics*. Kluwer Academic Publishers.
- Schenk, P., 2002. Thickness constraints on the icy shells of the Galilean satellites from a comparison of crater shapes. *Nature* 417, 419–421.
- Schenk, P., Matsuyama, I., Nimmo, F., 2008. True polar wander on Europa from global-scale small-circle depressions. *Nature* 453, 368–371.
- Schilling, N., Neubauer, F., Saur, J., 2007. Time-varying interaction of Europa with the jovian magnetosphere: Constraints on the conductivity of Europa's subsurface ocean. *Icarus* 192, 41–55.
- Schubert, G., Sohl, F., Husmann, H., 2009. Interior of Europa. In: Pappalardo, R., McKinnon, W., Khurana, K. (Eds.), *Europa*. Arizona Press Space Science Series, pp. 353–367.
- Schulson, E., 2001. Brittle failure of ice. *Eng. Fract. Mech.* 68, 1839–1887.
- Seidelmann, P. et al., 2007. Report of the IAU/IAG Working Group on cartographic coordinates and rotational elements: 2006. *Celest. Mech. Dyn. Astron.* 98, 155–180.
- Showman, A., Han, L., 2004. Numerical simulations of convection in Europas ice shell: Implications for surface features. *J. Geophys. Res.*, 109.
- Sohl, F., Spohn, T., Breuer, D., Nagel, K., 2002. Implications from Galileo observations on the interior structure and chemistry of the Galilean satellites. *Icarus* 157, 104–119.
- Sotin, C., Tobie, G., 2004. Internal structure and dynamics of the large icy satellites. *CR Phys.* 5, 769–780.
- Sotin, C., Tobie, G., Wahr, J., McKinnon, W., 2009. Tides and tidal heating on Europa. In: Pappalardo, R., McKinnon, W., Khurana, K. (Eds.), *Europa*. Arizona Press Space Science Series, pp. 85–117.
- Tobie, G., Choblet, G., Sotin, C., 2003. Tidally heated convection: Constraints on Europa's ice shell thickness. *J. Geophys. Res.* 108, 5124.
- Tobie, G., Mocquet, A., Sotin, C., 2005. Tidal dissipation within large icy satellites: Applications to Europa and Titan. *Icarus* 177, 534–549.
- Van Hoolst, T., Rambaux, N., Karatekin, O., Dehant, V., Rivoldini, A., 2008. The librations, shape, and icy shell of Europa. *Icarus* 195, 386–399.
- Wahr, J., Selvens, Z., Mullen, M., Barr, A., Collins, G., Selvens, M., Pappalardo, R., 2009. Modeling stresses on satellites due to nonsynchronous rotation and orbital eccentricity using gravitational potential theory. *Icarus* 200, 188–206.
- Wu, P., Peltier, W., 1982. Viscous gravitational relaxation. *Geophys. J. Roy. Astron. Soc.* 70, 435–485.
- Zimmer, C., Khurana, K., Kivelson, M., 2000. Subsurface oceans on Europa and Callisto: Constraints from Galileo magnetometer observations. *Icarus* 147, 329–347.